Galles, D., and Beckermann, C., "Measurement and Simulation of Distortion of a Steel Bracket Casting," in Proceedings of the 66th SFSA Technical and Operating Conference, Paper No. 5.2, Steel Founders' Society of America, Chicago, IL, 2012.

Measurement and Simulation of Distortion of a Steel Bracket Casting

D. Galles and C. Beckermann
Mechanical and Industrial Engineering Department, University of Iowa, Iowa City, Iowa 52242

Abstract

Casting distortion, caused by core expansion, is measured during *in situ* experiments involving a cast steel bracket. Additional measurements of various bracket features are taken after shakeout, and pattern allowances are subsequently calculated. Thermal simulations in MAGMAsoft[1] are performed, in which simulated and measured temperatures are matched. Temperature-dependent material properties are attained from a search of the literature and coupled with simulated thermal fields to resolve material properties at all times and locations throughout the cooling casting. Finally, distortions are predicted with the commercial software ABAQUS[2], in which a user-defined UMAT subroutine implements an elasto-visco-plastic constitutive model. Preliminary results show that the large bracket simulation predicts more distortion than was measured from the experiments, whereas the small bracket simulation predicts less. Because the distortions are strongly correlated to the thermal expansion of the core, additional research of the mold properties is needed to improve agreement.

1. Introduction

During cooling of a steel casting, thermal strains create interactions at the mold-metal interface and generate stresses. These stresses induce mechanical strains, which in turn may cause gross distortions. Furthermore, if the stresses arise before solidification is complete, hot tears may form, which are irreversible cracks that develop in the semi-solid mushy zone[3]. Distortions and defects compromise the quality of the casting and may require costly, time-consuming rework or scrapping of the part, significantly impacting the profitability of the foundry. A thorough understanding of the material behavior in both the casting and mold is essential to minimize the aforementioned issues. In recent years, thermal simulation software has been coupled with advanced stress models to predict stresses and deformations during solidification and cooling. However, these models are still unproven, due in part to the limited availability of high-temperature material property data from the literature.

Because the microstructure created during solidification differs from that of a reheated specimen, stress models should be validated by data collected from *in situ* experiments. However, because displacement in castings at high temperatures is difficult to measure, studies which use *in situ* tests in conjunction with computational stress models are limited. Galles *et al.*[4] measured and predicted distortion of a steel bar in which strains were induced with the aid of a turnbuckle and restraint. Monroe and Beckermann[5] performed *in situ* experiments of a steel bar to predict hot tearing.

In this study, *in situ* casting experiments of a steel bracket are performed to measure casting distortion. The distortions result from mechanical interactions at the mold-metal interface, due to the combination of core expansion and steel contraction. Displacement transducers measure the distortion at a single location on the bracket as a function of time. Pattern allowances are calculated at several feature locations by

subtracting the final casting dimensional measurement after shakeout from the initial mold measurement. Additionally, temperatures as a function of time are recorded in both the steel and core using thermocouples. Thermal simulations are performed in MAGMAsoft, in which simulated measured temperatures are matched and temperature fields are generated at discreet time steps from pouring down to room temperature. To predict distortions, stress simulations are performed with the commercial software ABAQUS, in which a user-defined UMAT subroutine implements an elasto-visco-plastic constitutive model. Temperature-dependent material properties are acquired through a search of the literature. By transferring the thermal fields from MAGMAsoft to the ABAQUS mesh, these properties are now known at all times and locations of the bracket during cooling. Finally, the model is validated through a comparison of predicted and measured distortions.

2. Description of Experiments

2.1 Experimental Setup

To create mechanical interactions at the mold-metal interface, a bracket-shaped geometry with a core was designed. Two geometries, shown in Figure 1, were produced from each experimental set. Other than their core widths, the large (4 inches) and small (1 inch) brackets have identical dimensions. By varying the core sizes, the heating rates (and core expansion) will be different for the two brackets, resulting in different amounts of distortion. To estimate the heating rates in the core, a preliminary MAGMAsoft simulation predicted temperature fields shortly after pouring, as shown in Figure 2.

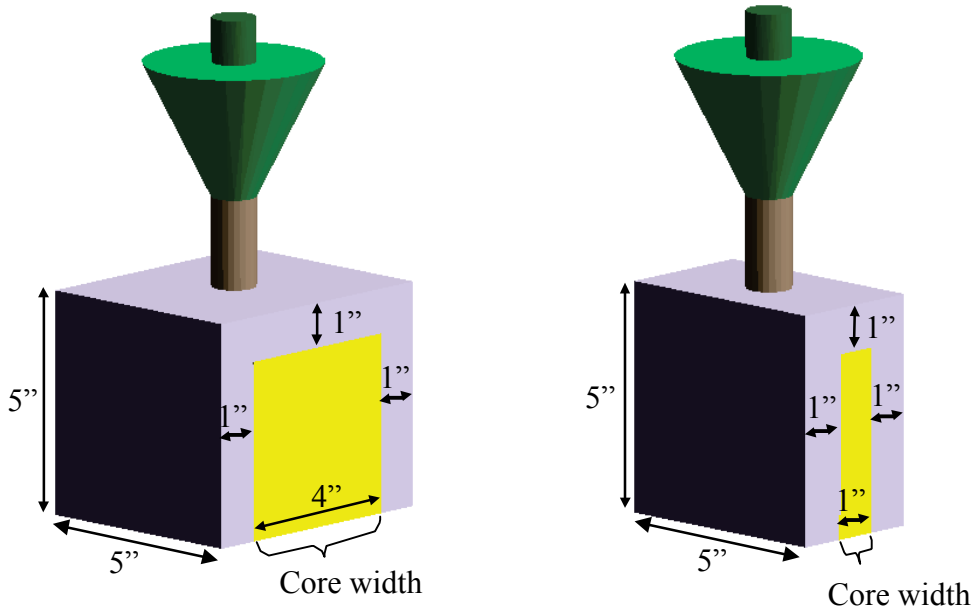

a) Large bracket

b) Small bracket

Figure 1. Bracket geometry. The large and small brackets only differ in the size of the core widths.

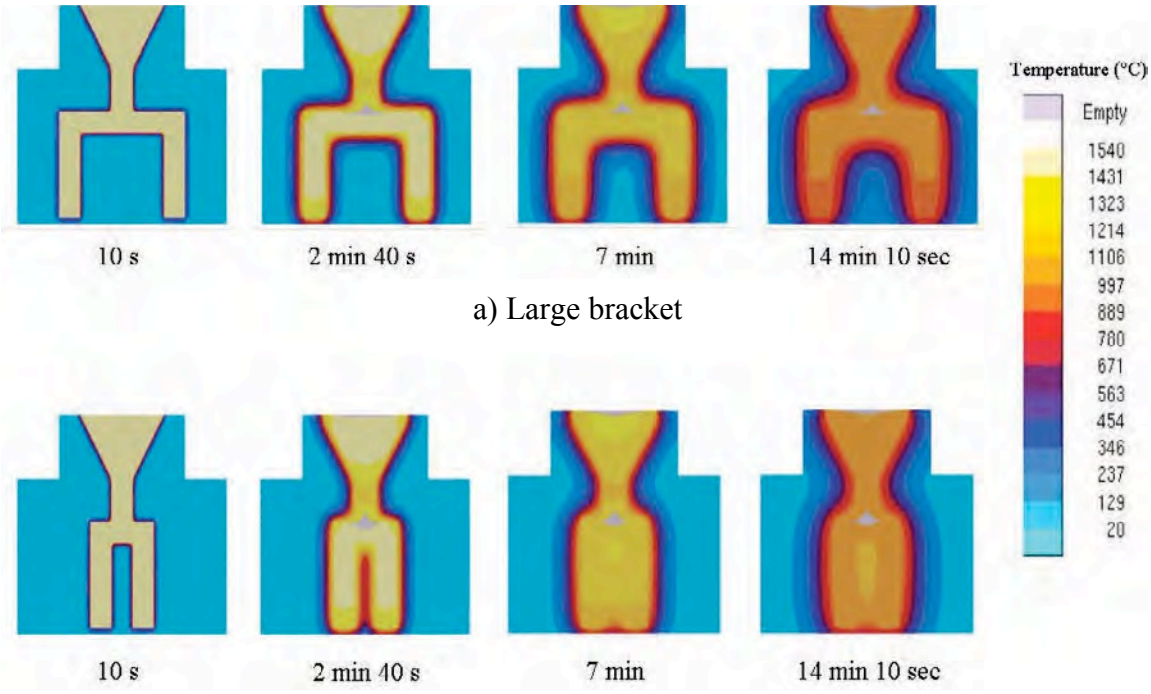

Figure 2. Preliminary simulated thermal fields at the mid-plane of the castings. The core of the small bracket heats much more rapidly than the large core, which will result in different casting conditions between the two bracket sizes.

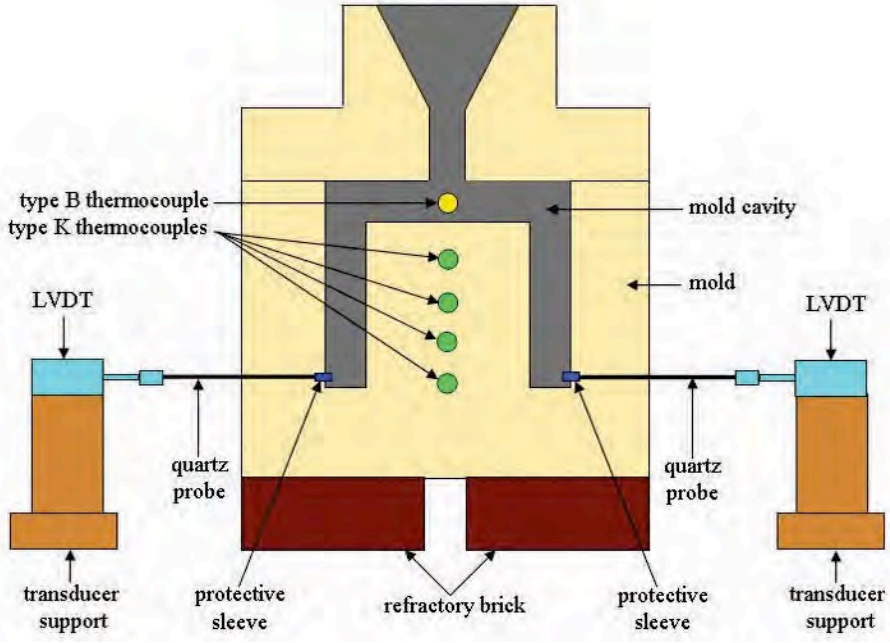

Figure 3. Experimental schematic of large bracket casting at mid-plane. All data measurements are taken at the mid-plane. Displacement measurements are taken with LVDT's located 5 mm from the bottom of each leg. A type B thermocouple located under the sprue records the temperature in the steel, and type K thermocouples located in the middle of the core record the sand temperatures.

Figure 2(b) shows the small bracket core is nearly in thermal equilibrium with the casting after 7 minutes, while the large casting, shown in Figure 2(a), is still relatively cold in the center of the core even after 14 minutes. While the simulation is only a first approximation and may not be entirely accurate, it still gives insight to the different thermal conditions that will exist in the cores during casting.

A schematic of the large bracket casting is shown in Figure 3. Displacement as a function of time was measured using LVDT's (linear variable differential transformer) located 5 mm from the bottom of each bracket leg at the mid-plane of the casting. Because an LVDT cannot withstand the high temperatures encountered in casting conditions, fused quartz rods were used to transmit displacement from the casting to the LVDT. The thermal expansion of fused quartz is negligible when compared to steel, making it a suitable material for this application. The drawback of fused quartz, however, is its susceptibility to brittle fracture. To combat this, metal sleeves were placed over the quartz rod ends in direct contact with the casting, protecting them from compressive forces as the casting thermally contracts. Additionally, digital calipers were used to take mold measurements, termed outer length (L) and gap opening (G) at the bottom (b), middle (m), and top (t) of the bracket legs and on face 1, face 2, and the mid- plane, as shown in Figure 4. Leg thicknesses (T) were subsequently calculated using the

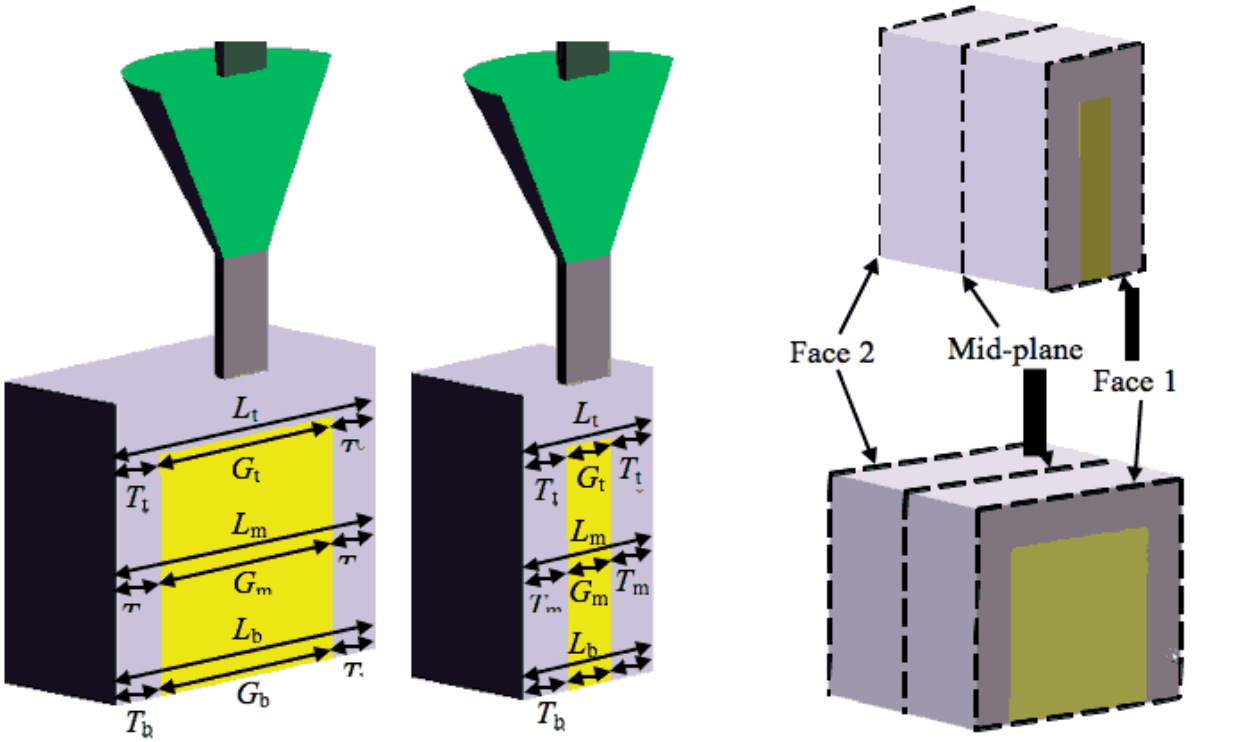

(a) Locations of measurements on each face (b) Measured faces Figure

Figure 4. Mold and final casting measurements were taken of the outer bracket length, *L*, and bracket gap opening, *G*, at the bottom (b), middle (m), and top (t) of the bracket legs at face 1,
face 2, and the mid-plane. Mold measurements of leg thicknesses, *L*, were calculated using the relation (*L*-*G*)/2.

relation (*L*-*G*)/2. Temperature measurements as a function of time were also taken at the mid-plane. The steel temperature was taken with a type-B thermocouple located directly under the sprue, while mold temperatures were taken with type-K thermocouples located at different heights in the center of the core. Mold dimensions and thermocouple placements are shown in Figure 5.

Experimental sets were performed at the University of Northern Iowa's Metal Casting Center. The castings of each experimental set were produced from a 250 lb heat and prepared in an induction furnace. The casting chemistry for the sets, shown in Table 1, was targeted as WCB carbon steel. While silica sand was used to construct the molds in all sets, the binder systems were changed after set 2. Sets 1 and 2 used the Zealign bio-urethane binder system with a 60/40 ratio and 8% catalyst, whereas sets 3 and 4 used the Pepset phenolic-urethane binder system with a 55/45 ratio and 6% catalyst. An image of the final castings is shown in Figure 6.

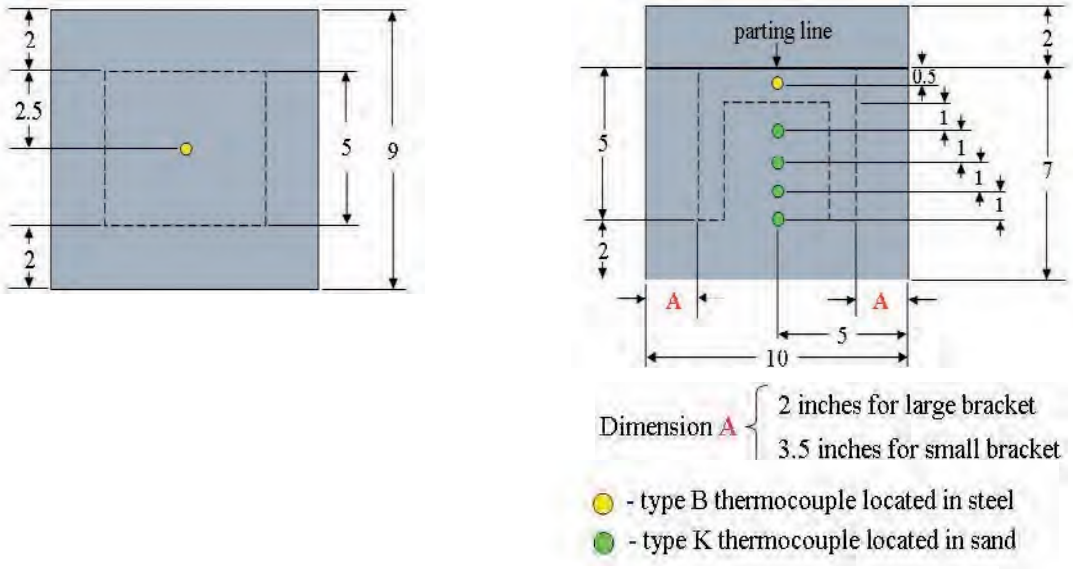

a) Top view b) Front view

Figure 5. Mold dimensions and thermocouple placements. All units in inches.

Table 1. Casting chemistry.

Casting Chemistry											
Set	**%C**	**%Si**	**%Mn**	**%P**	**%S**	**%Cr**	**%Mo**	**%Ni**	**%Al**	**%Cu**	**%Fe**
1	0.30	0.57	0.41	0.031	0.026	0.01	0.00	0.00	0.056	0.01	98.56
2	0.33	0.59	0.39	0.015	0.020	0.01	0.01	0.01	0.069	0.03	98.52
3	0.27	0.23	0.61	0.12	0.009	0.63	0.19	2.0	0.021	0.04	95.84
4	0.14	0.38	0.26	0.093	0.013	0.02	0.01	0.01	0.001	0.07	98.98

Figure 6. Final castings.

2.2 Experimental results

All temperature results are shown on large (60000 s), medium (5000 s) and small (400 s) time scales. Steel temperatures as a function of time for the large and small brackets are shown in Figures 7 and 8, respectively. The corresponding cooling rates of the steel, which were calculated as the negative temperature change per sampling period ($-\Delta T/P_{sample}$), are plotted as a function of temperature and shown in Figure 9. The cooling rate curves were smoothed using a 21-point running average. The temperature evolution recorded by the steel thermocouple is understood by the following events. When the molten steel is poured into the mold, the thermocouple immediately begins to read an increasing temperature. However, due to the physical limitations of the thermocouple material, a lag time of several seconds passes before the actual temperature is read. For this reason, the maximum temperature is read 10-20 seconds after pouring, as shown in Figures 7(c) and 8(c). From this maximum, the steel rapidly cools until the onset of solidification at the liquidus temperature, T_{liq}. At this temperature, the phase change from liquid to solid produces an abundance of latent heat, reducing the cooling rate to (nearly) zero and causing the temperature to become (nearly) constant with time. The liquidus temperature is experimentally determined as the temperature at this minimum cooling rate. The average liquidus temperature, $T_{liq,average}$, for all sets was 1499°C. As the steel continues to solidify, more latent heat is released, albeit at slower rate, resulting in an increased cooling rate. The cooling rate reaches a maximum when the steel has completely solidified and the last amount of latent heat has been released. The

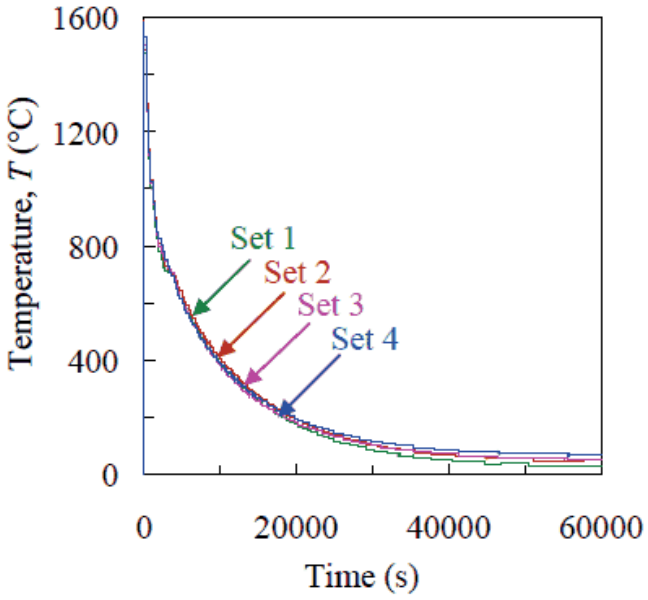

(a) Large time scale.

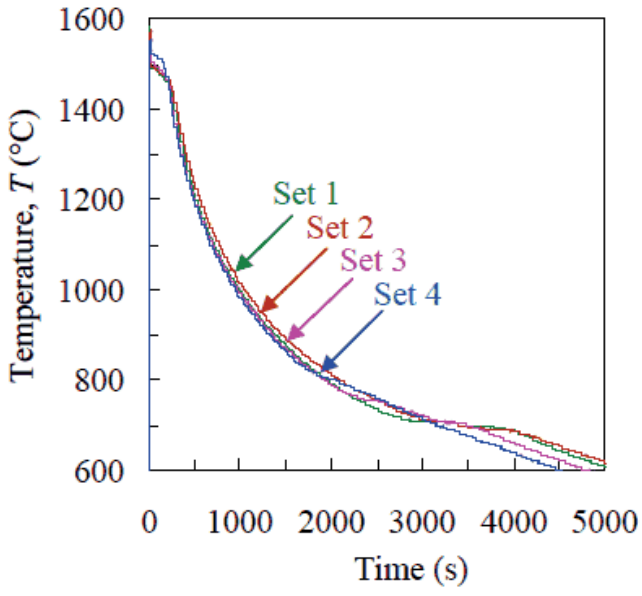

(b) Medium time scale.

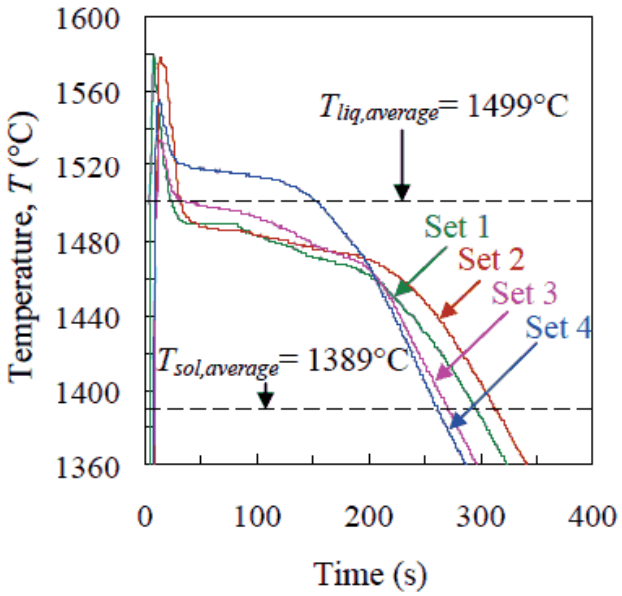

(c) Small time scale.

Figure 7. Large bracket measured steel temperatures.

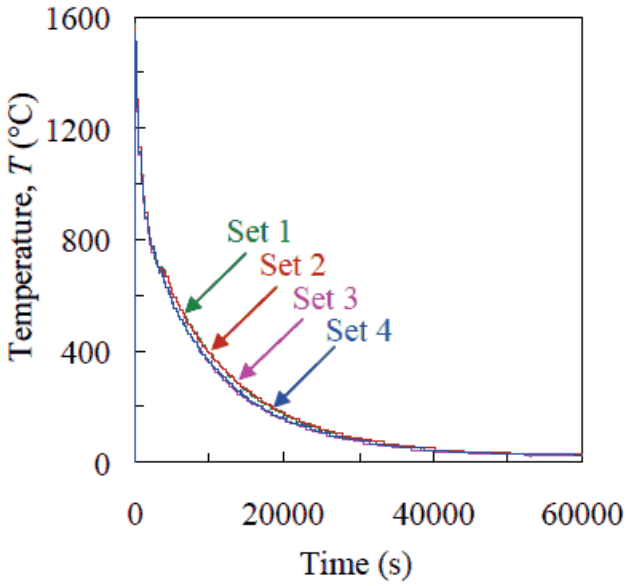

(a) Large time scale.

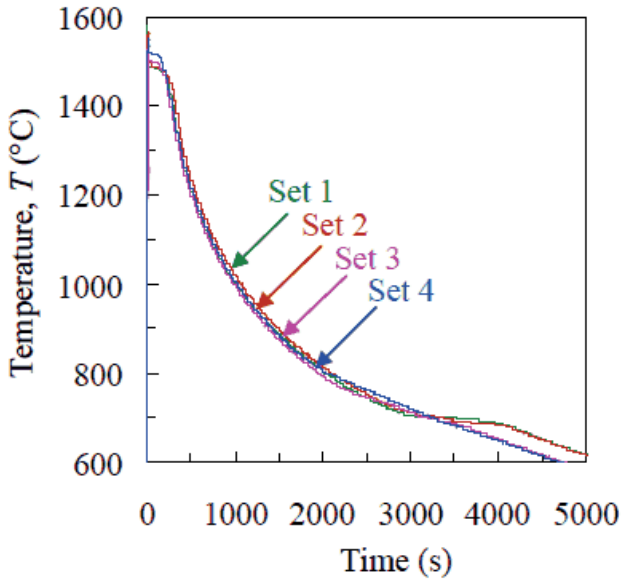

(b) Medium time scale.

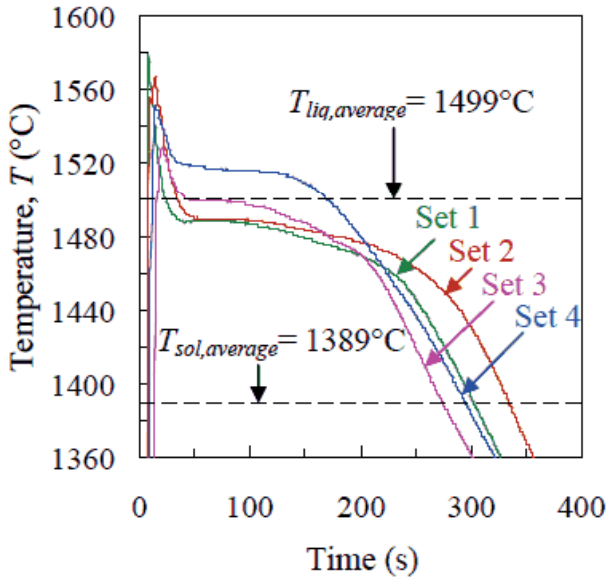

(c) Small time scale.

Figure 8. Small bracket measured steel temperatures.

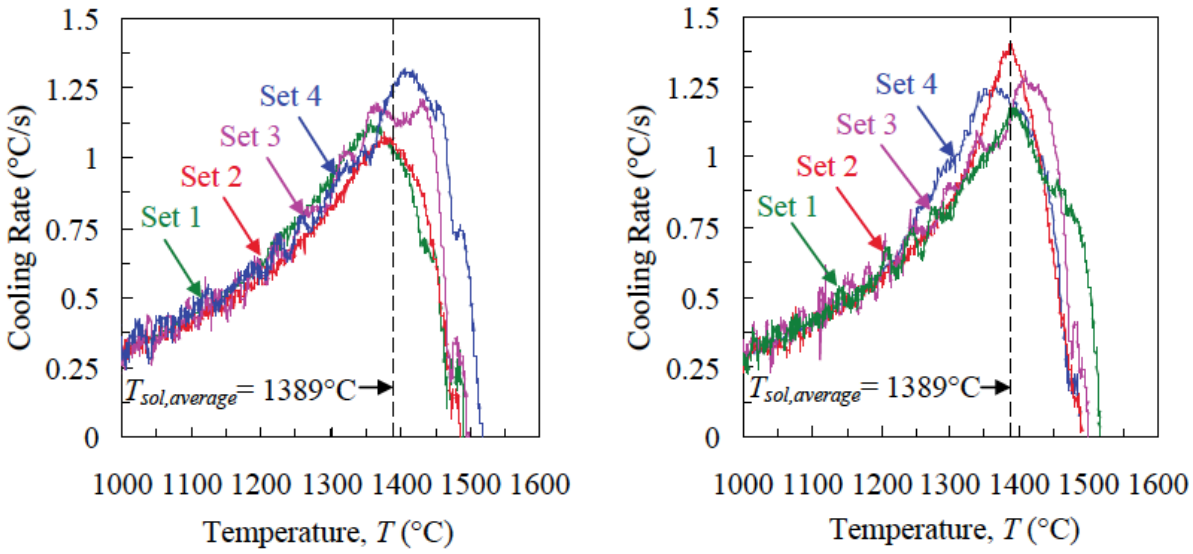

Figure 9. Bracket cooling rates.

corresponding temperature at this maximum is the solidus temperature, T_{sol}. The average solidus temperature for all sets, shown as the vertical dashed lines in Figures 9(a) and 9(b), was 1389°C. When the casting cools below 800°C, two additional phase transformations occur in which the austenitic steel decomposes into 1) proeutectoid ferrite and 2) pearlite. Depending on the casting chemistry, the temperature difference between these transformations varies from a few degrees to over 100°C. Due to the release of latent heat, these transformations can be seen as temperature arrests ranging from 650°C to 800°C in Figures 7(b) and 8(b). After these transformations, the temperature spontaneously cools to room temperature. In general, temperature differences between experiments can be seen on the small and medium time scales. However, when viewed on the large time, the temperatures for all sets are similar, showing good repeatability, regardless of variations in the casting chemistry. The significance of this agreement is that a single thermal simulation is needed to adequately describe the temperature evolution of all experimental sets.

Mold temperatures as a function of time for the large and small brackets are shown in Figures 10 and 11, respectively. Temperatures were recorded at 4 locations in the core, shown in Figures 10(d) and 11(d). Location 1 and 2 temperatures were recorded from set 3, whereas location 3 and 4 temperatures are from set 4. Mold thermocouples were not used in sets 1 and 2. The temperatures in the center of the core (Location 2) for the large and small brackets reach approximate maximum values of 650°C at 2500 s and 1200°C at 500 s, respectively. Hence, the small bracket core not only reaches a much higher temperature but also reaches it much sooner than the large bracket core. This confirms, as predicted in the preliminary MAGMAsoft simulation (shown in Figure 2) that the core heating rates are very sensitive to core size. The mold temperature evolution is straightforward to explain, with one exception. As the sand heats up, the binder absorbs heat, eventually resulting in an endothermic reaction that burns away the binder.

This reaction can be seen as a "kink" in the mold temperature curves near 200°C in Figures 10(b) and 11(c). Other than this reaction, the mold heats up monotonically until it reaches thermal equilibrium with casting, at which time it cools monotonically to room temperature.

The large bracket LVDT outer length, shown in Figure 12(d), was calculated by adding the LVDT displacements of both bracket legs. Results are shown on large, medium, and small time scales in Figures 12(a) – 12(c). An increasing outer length with time reflects expansion of the bracket legs outward. However, the decrease of LVDT outer length in the first 50 seconds, shown Figure 12(c), is due to another phenomenon and requires explanation. Immediately after pouring, the mold material close to the casting experiences rapid heating, resulting in thermal expansion. The casting, which is still mostly liquid and unable to transmit stresses, offers no resistance to this expansion. As a result, the mold compresses the liquid metal, forcing it out of the mold and back into the pouring cup, effectively reducing the volume of the casting. This effect can be seen as a decrease in the LVDT outer length. Within a few seconds, however, an outer shell solidifies, and the expanding mold can no longer compress the casting. After approximately 100 s, the LVDT outer length begins to increase, explained by the following. As the core initially expands during heating, the tensile forces in the outer mold provide resistance. However, because the compressive strength of sand is far superior to its tensile strength, the increasing compressive forces (due to the thermally expanding core) eventually overcome the tensile forces, resulting in fracture of the outer mold. Also, because the steel is still very weak at these high temperatures and provides little resistance, the core essentially expands freely and pushes the bracket legs outward. An important caveat, however, is that the bracket continues to thermally contract during this core expansion. In particular, contractions in the bracket reduce the leg thickness and should decrease the LVDT outer length. However, these contractions are small when compared to the core expansion, and as a result, the LVDT outer length increases. After approximately 1000 s, the LVDT outer length reaches a maximum and begins to decrease as a result of 1) thermal contractions in the core as the core begins to cool and 2) thermal contractions in the bracket legs. The contracting bracket legs, which had a small effect on the LVDT outer length during core expansion, now have a significant impact on the outer length and may account for the majority of the decrease in LVDT outer length from 1000 s until the next minimum. Depending on the set, the LVDT outer length reaches a minimum between 1500 and 2500 s, seen in Figure 12(b). This minimum denotes the beginning of the solid state transformations, during which a sharp decrease in the steel density causes an increase of the casting volume and increases the LVDT outer length. Due to temperature gradients in the casting, the solid state transformations occur at different times throughout the bracket, resulting in an increase of the LVDT outer length for 1000 – 1500 s (depending on the set). At the end of the solid state transformations, the LVDT outer length reaches a second maximum. Because the steel significantly increases in strength during the transformations, the compressive forces of the core can no longer resist the thermally contracting steel, and the measured displacement between the final solid state transformation and room temperature is simply free contraction of the steel. The evolution of the small bracket LVDT outer length, shown in Figure 13, is similar to the large bracket. The only differences between the large and small bracket

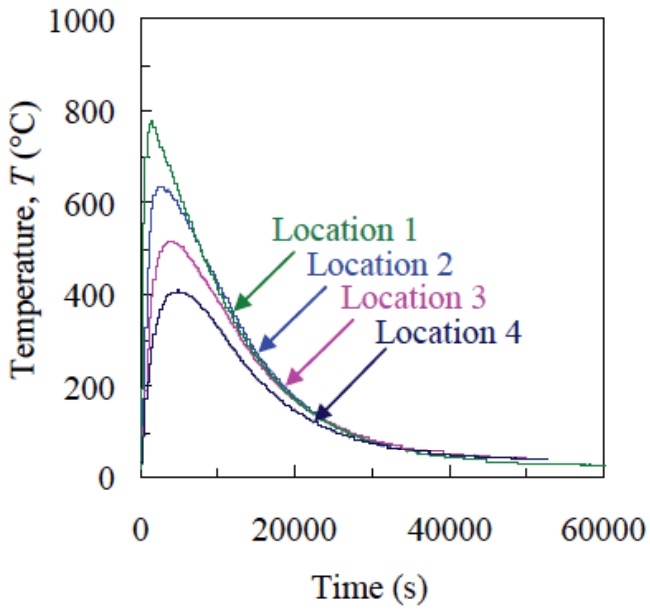

(a) Large time scale.

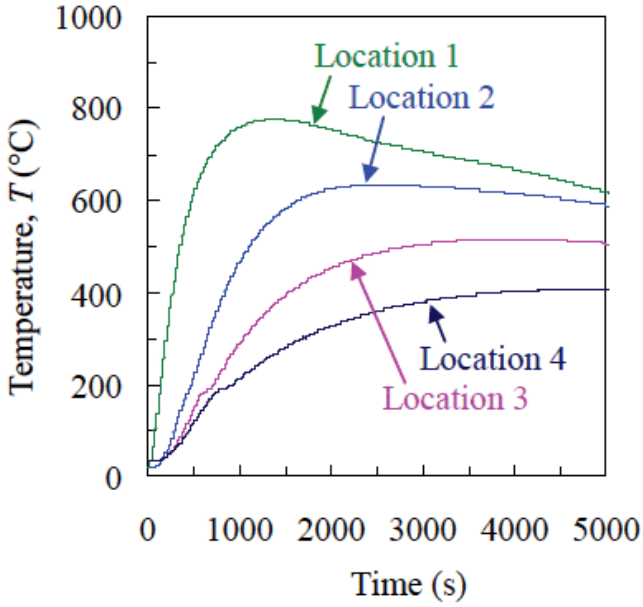

(b) Medium time scale.

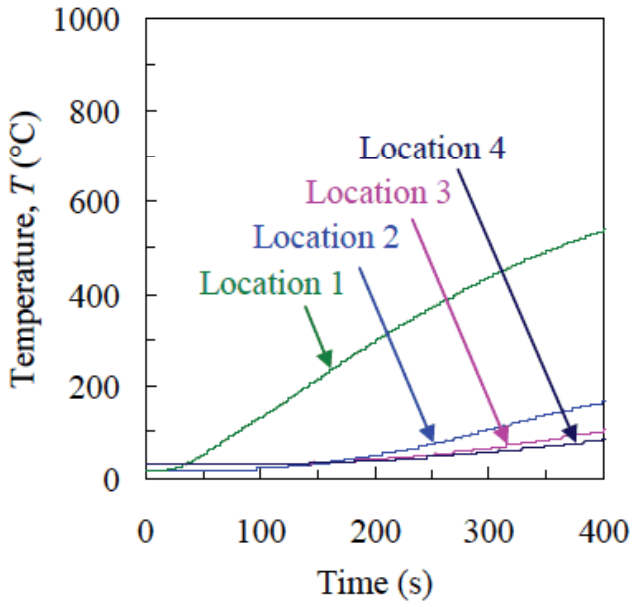

(c) Small time scale.

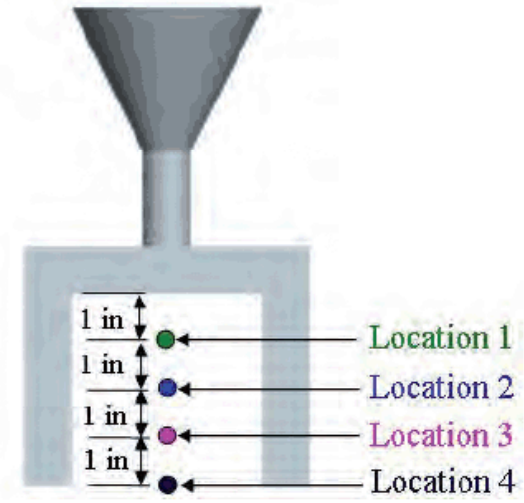

(d) Sand Thermocouple locations

Figure 10. Large bracket measured sand temperatures.

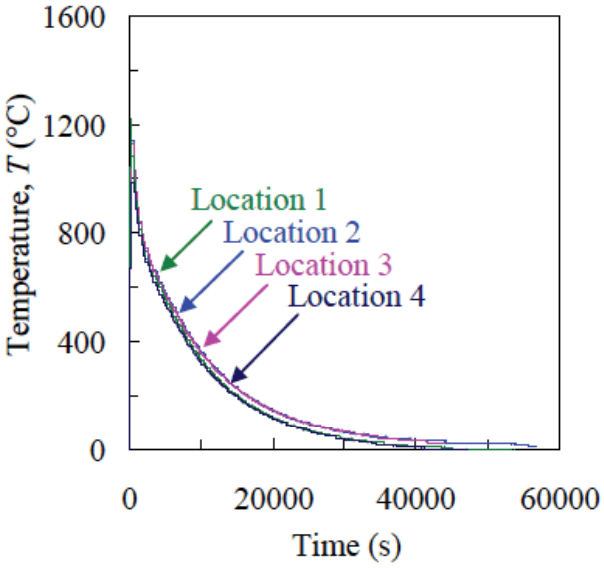

(a) Large time scale.

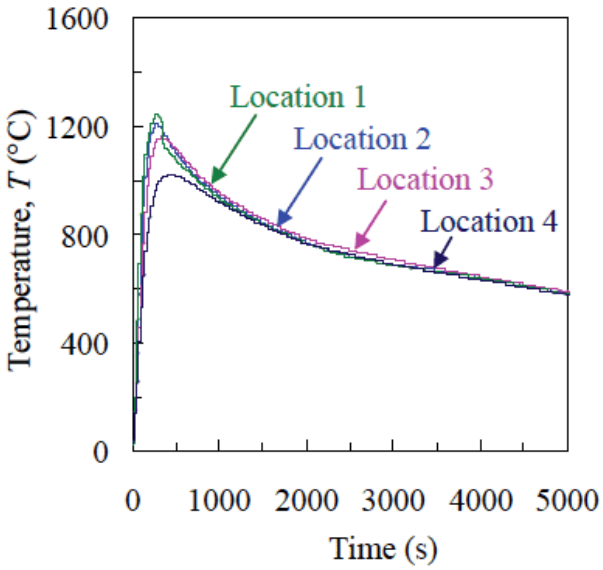

(b) Medium time scale.

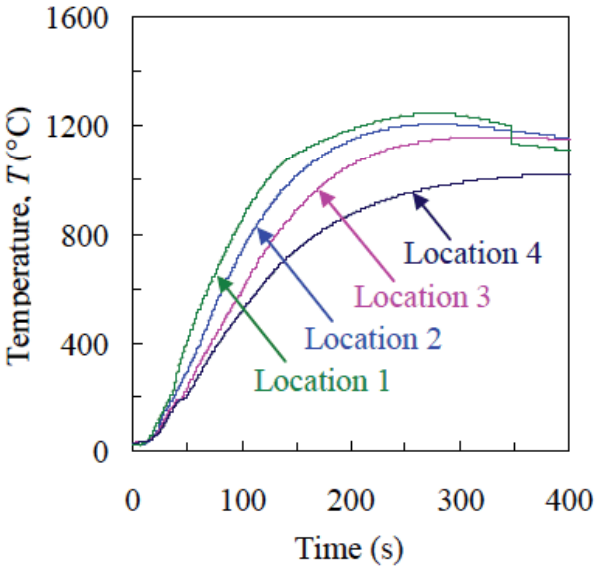

(c) Small time scale.

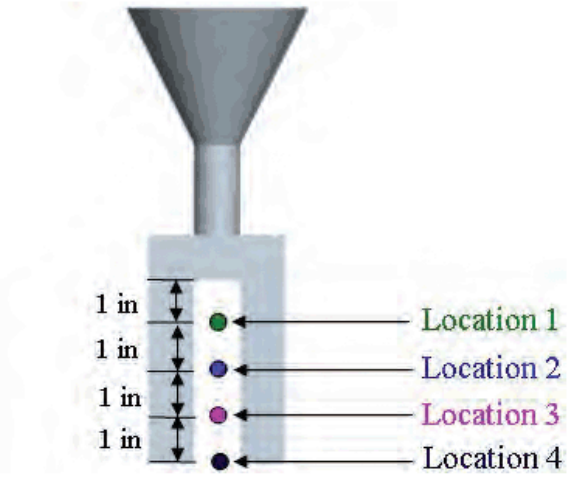

(d) Sand Thermocouple locations

Figure 11. Small bracket measured sand temperatures.

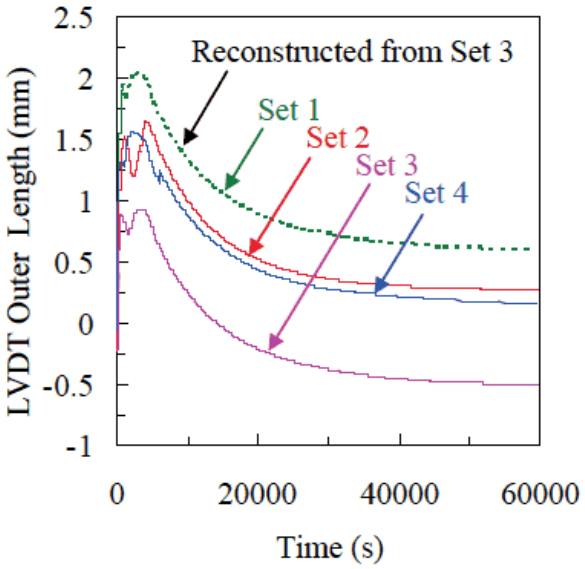

(a) Large time scale.

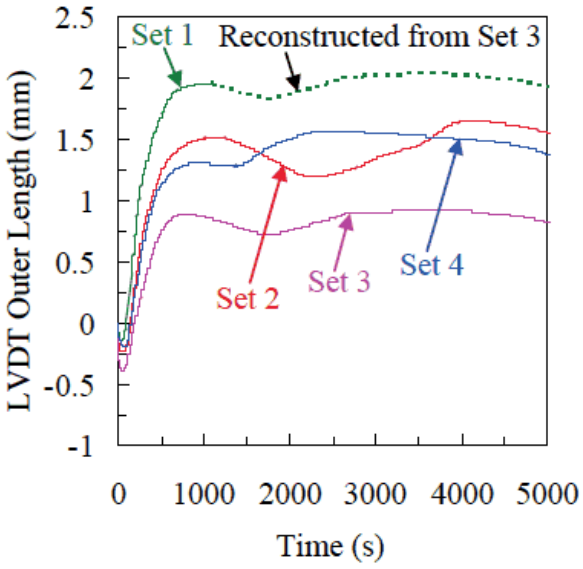

(b) Medium time scale.

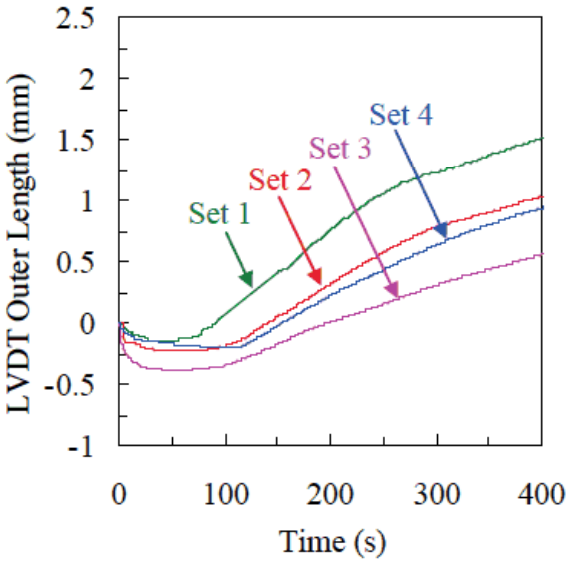

(c) Small time scale.

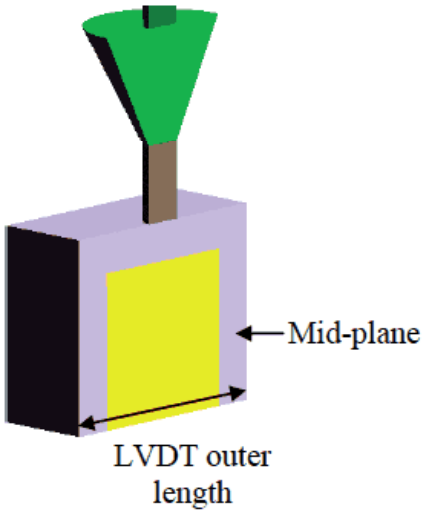

(d) LVDT measurement location

Figure 12. Large bracket LVDT results.

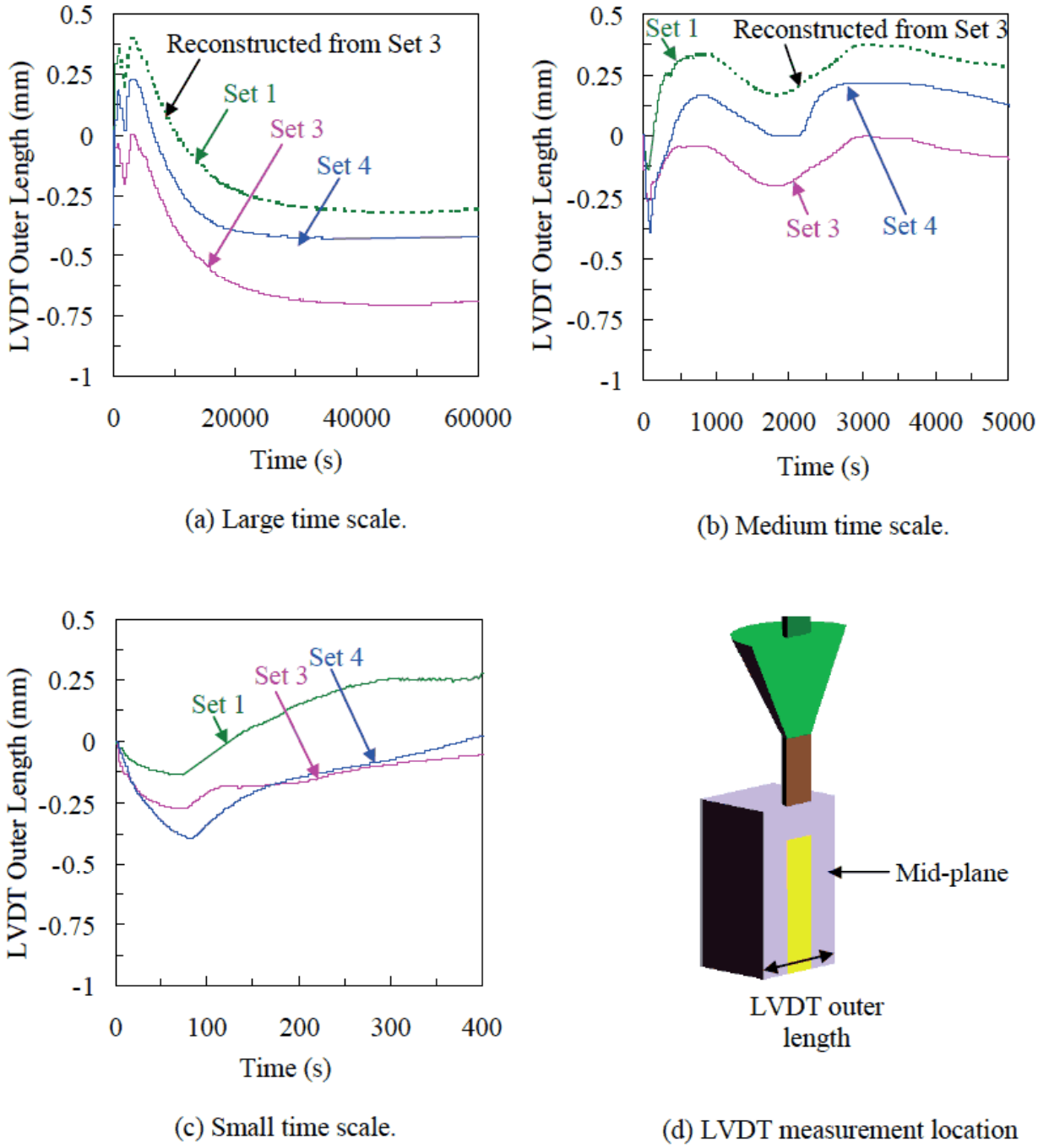

(a) Large time scale.

(b) Medium time scale.

(c) Small time scale.

(d) LVDT measurement location

Figure 13. Small bracket LVDT results.

LVDT displacement evolutions are the times and magnitudes of the minimums and maximums, which is due to the different thermal conditions in the cores during cooling.

After shakeout, final casting measurements were taken with digital calipers at the locations shown in Figure 4(a) on face 1, face 2, and the mid-plane. The dimensional differences of all large and small bracket sets were calculated by subtracting the mold measurements from the final casting measurements, as shown in Figures 14 and 15, respectively. The averaged dimensional differences over the outer (face 1 and face 2),

mid-plane, and overall (face 1, face 2, and mid-plane) faces for the large and small brackets, are shown in Figures 16 and 17, respectively. For both large and small brackets, the gap openings, G (location shown in figure 4), are positive values at the bottom (b) and middle (m) leg locations, which shows the bracket legs experienced significant distortion as a result of being pushed outward by the core during heating of the mold. In addition, distortional variations can be seen between the mid-plane and outer planes. In particular, the gap opening at the middle location, G_{m}, experienced more distortion more at the mid-plane than the outer planes, resulting in a larger positive dimensional difference at the mid-plane. Because of this variation, the bracket legs have a slight concave shape. While the bracket leg thicknesses may be expected to shrink freely, Figures 17 and 18 show the magnitudes increase from the bottom to top of the legs. Therefore, the bracket leg thicknesses also experience distortions.

From Figure 4(a), it can be seen that the bracket dimensions are related by the expression $L = G + 2T$. However, the plot of L vs. $G + 2T$ for the large and small brackets in Figure 18 shows (1) these values (L and $G + 2T$) are generally not equal, and (2) a bias exists, in which $L < G + 2T$. Because there is an uncertainty associated with taking measurements from a rough casting surface, some scatter is expected about the zero line. However, this does not explain why the majority of points lie to the right of the zero line. This bias can be explained by sand penetration. During casting, sand particles at the mold-metal interface penetrate into the casting. While some grains are completely embedded in the casting, others only partially penetrate it, while the remainder of the grain protrudes out of the casting surface. As a result, measurements taken from this surface are larger than if no sand penetration had occurred. Therefore, due to sand penetration, the sum of the three measurements on the horizontal axis in Figures 18(a) and 18(b) is larger than the single measurement on the vertical axis. As a result, most points lie to the right of the zero line. Standard deviations of the symbols from the zero line for the large and small brackets were calculated to be 0.27 and 0.24 mm, respectively.

Similarly, the dimensional differences (*dif*) between the mold and final casting have the relation $L_{dif} = G_{dif} + 2T_{dif}$. A plot of L_{dif} vs. $G_{dif} + 2T_{dif}$ is shown for the large and small brackets in Figure 19. Similar to Figure 18, a bias is seen for both large bracket and small bracket dimensional differences, which is also explained by sand penetration.

Because the LVDT outer length at room temperature measures the same dimension as the dimensional difference of L_{b} at the mid-plane, the two measurements are compared for all large and small bracket experiments and shown in Figure 20. Each symbol in the plot refers to the LVDT vs. $L_{b,dif}$ measurement of each set. For measurements of equal value, the plotted symbol will lie on the zero line. However, due to the rough casting surface, an uncertainty is associated with measurements of $L_{b,dif}$ (taken with digital calipers). Even with these uncertainties, however, the symbols still lie near the zero line, with a slight bias due to sand penetration. This comparison validates the accuracy (within the uncertainty of the digital calipers measurements) of both measurement devices (LVDT and digital calipers) used in this study.

The dimensions L, G, and T (shown in Figure 4(a)) located at the bottom (b), middle (m), and top (t) of each bracket face can be viewed as features of the casting. By measuring the pattern allowances at these features, the distortion of the entire bracket can

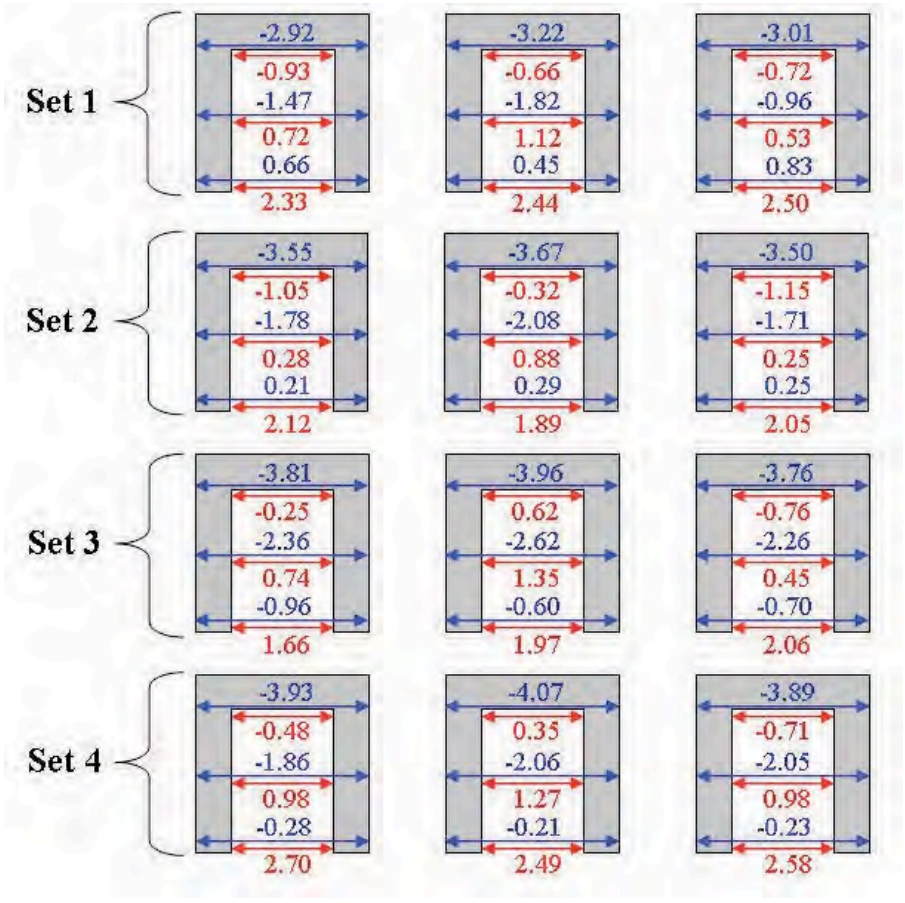

(a) Face 2 (b) Mid-plane (c) Face 1

Figure 14. Large bracket dimensional differences from all sets. Dimensional differences were calculated by subtracting initial mold measurements from final casting measurements after shakeout. All units are in mm.

be summarized concisely. Figure 21 shows the pattern allowance of each feature on all faces (face 1, face 2, and mid-plane) and experimental sets, resulting in 12 data points for each feature. Positive pattern allowances represent contractions. The free shrink value of 2.2% was determined from the unrestrained steel bar contractions in Galles *et al*[4]. From the figure, it can be seen that there are a wide range of pattern allowances. The left portion of Figure 21 shows the leg thicknesses have the largest pattern allowances, ranging from 2% to 10%. A significant amount of this contraction likely occurs in the first few seconds after pouring, when the expanding mold compresses the casting to force the molten steel back into the pouring cup, increasing the pattern allowance. The gap opening pattern allowances, conversely, are largely negative and range from -8% to 1%. These negative values are the result of core expansion, which pushes the bracket legs

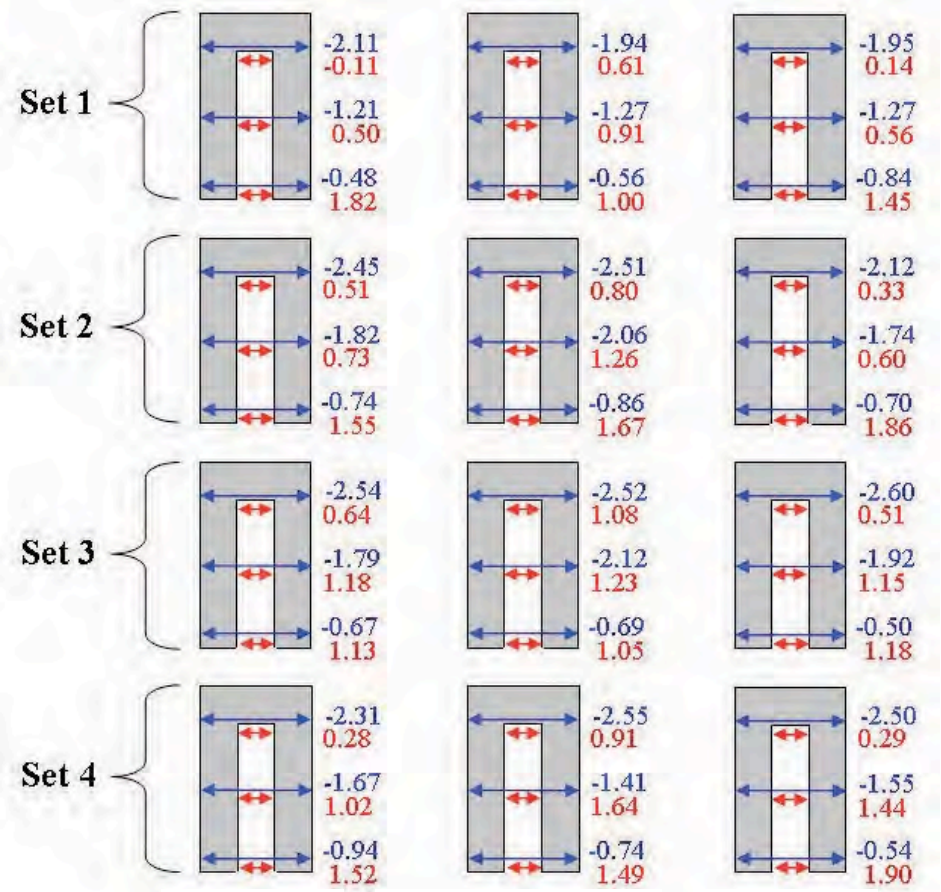

(a) Face 2 (b) Mid-plane (c) Face 1

Figure 15. Small bracket dimensional differences from all sets. Dimensional differences were calculated by subtracting initial mold measurements from final casting measurements after shakeout. All units are in mm.

outward. To explain the pattern allowances for the outer length (L), Recall from Figure 4(a) that the dimensions are related by $L = G + 2T$. From this expression, it is evident that the pattern allowance of the outer length is a function of the leg thickness and gap opening pattern allowances. Therefore, the outer length pattern allowance will fall somewhere in between the leg thickness and gap opening pattern allowances. Coincidentally, most of the outer length pattern allowances are close to the free shrink line. If pattern allowances had only been measured at the outer length, the large amounts of distortion in the bracket may not have been realized. Therefore, the locations at which pattern allowances are measured are critical in characterizing the distortion. The standard deviations vary significantly in Figure 21. The leg thicknesses and gap opening of the small bracket have the largest standard deviations. The reason for these large values is the length of these three features (1 inch) is relatively small. Therefore, distortions will have large effects on the pattern allowances and likely result in a larger standard deviation.

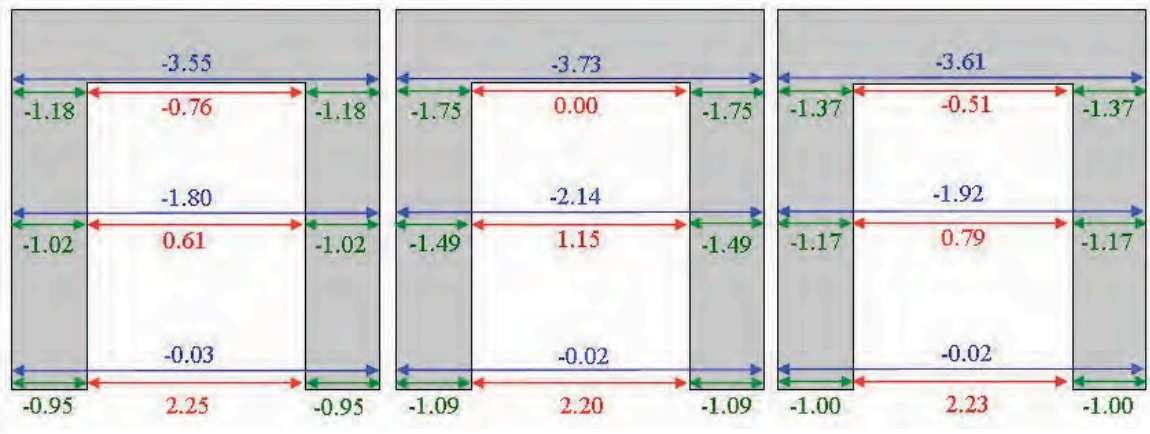

(a) Outer faces (b) Mid-plane (c) Overall

Figure 16. Large bracket dimensional differences from Figure 14 are shown as outer face (face1 and face 2), mid-plane, and overall (face 1, face 2, and the mid-plane) averages. The positive values of gap opening, *G* (location shown in Figure 4), at the bottom and middle of the bracket legs show the distortions as a result of core expansion. All values have units of mm.

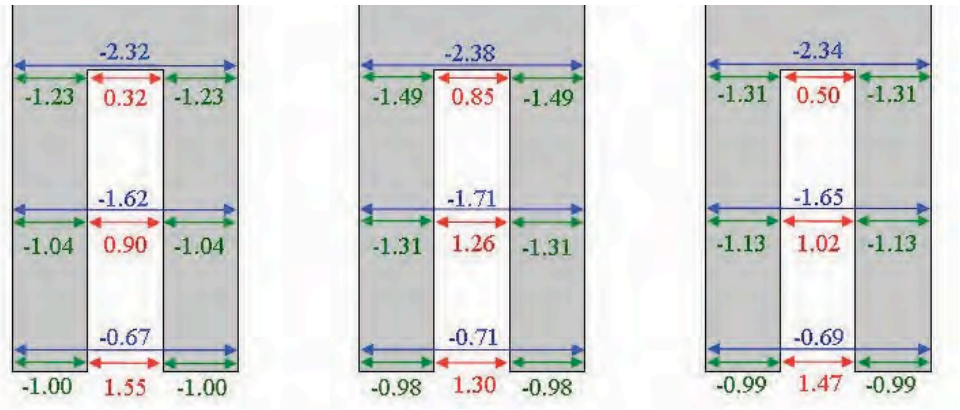

(a) Outer faces (b) Mid-plane (c) Overall

Figure 17. Small bracket dimensional differences from Figure 15 are shown as outer face (face1 and face 2), mid-plane, and overall (face 1, face 2, and the mid-plane) averages. The positive values of gap opening, *G* (location shown in Figure 4), at the bottom and middle of the bracket legs are distortions resulting from core expansion. All values have units of mm.

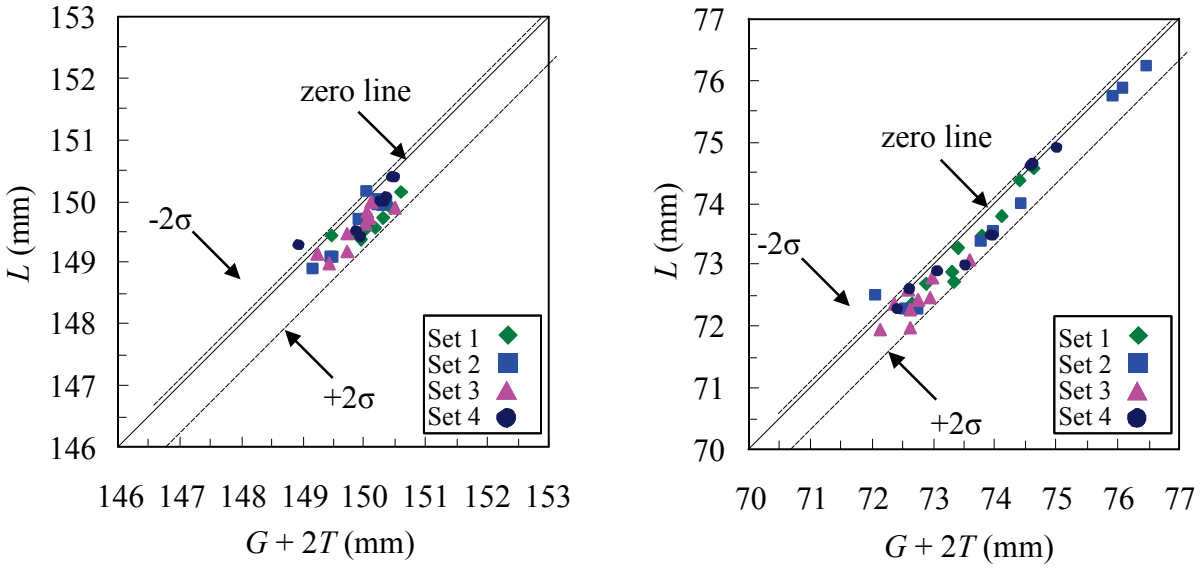

(a) Large bracket (b) Small bracket

Figure 18. The final dimension of the outer length, L, is plotted vs. $G + 2T$ of the large and small brackets. From Figure 4, it can be seen that the bracket dimensions are related by $L=G+2T$. The standard deviations of the large and small brackets are 0.27 and 0.24 mm, respectively. A bias, which can be seen as the majority of the points lying right of the zero line, is a result of sand penetration into the casting surface.

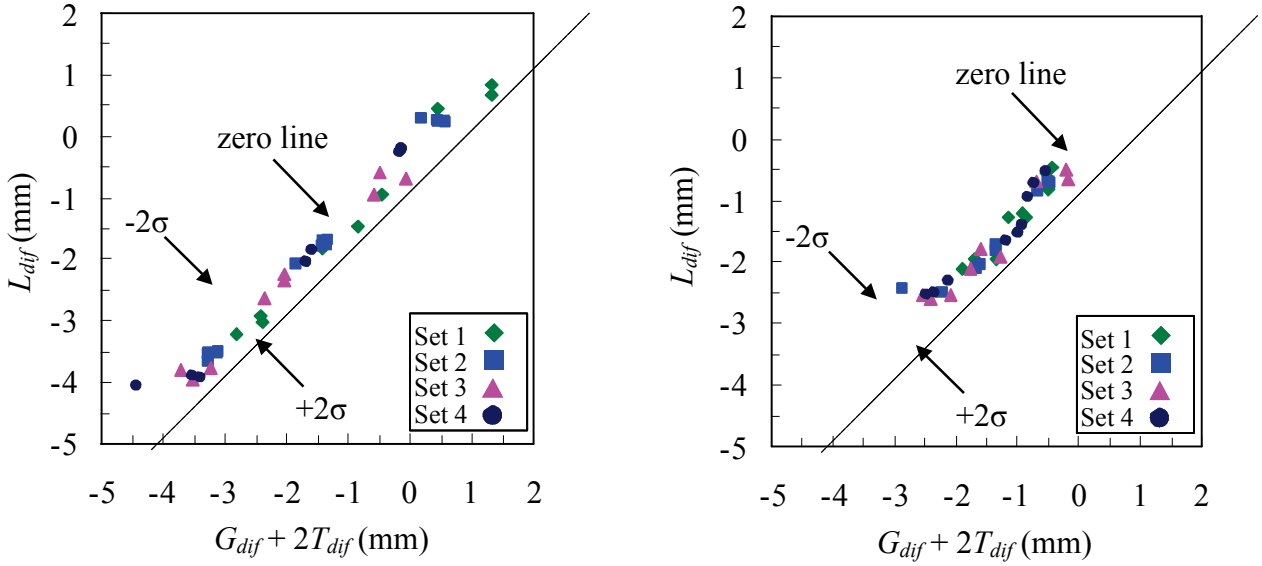

(a) Large bracket (b) Small bracket

Figure 19. The dimensional differences (*dif*) of the outer length, L_{dif}, are compared to the sum $G_{dif} + 2T_{dif}$ of the large and small brackets. From Figure 4, it can be seen that the bracket dimensions are related by $L=G+2T$. The standard deviations of the large and small brackets are 0.28 and 0.24 mm, respectively. A bias, which can be seen as the majority of the points lying right of the zero line, is a result of sand penetration into the casting surface.

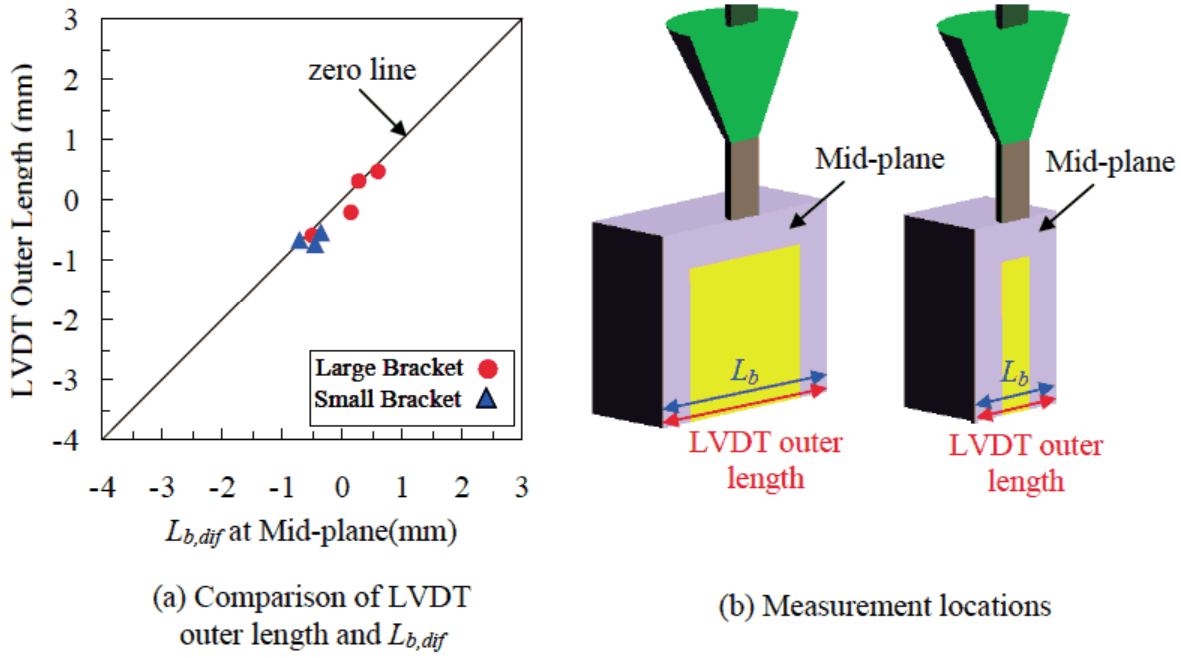

(a) Comparison of LVDT outer length and $L_{b,dif}$

(b) Measurement locations

Figure 20. The LVDT outer length is plotted vs. L_b at the mid-plane for all large and small experimental sets. These measurements were taken at the same location with different devices (LVDT and digital calipers). A small bias, which can be seen as the majority of the points lying right of the zero line, is a result of sand penetration into the casting surface.

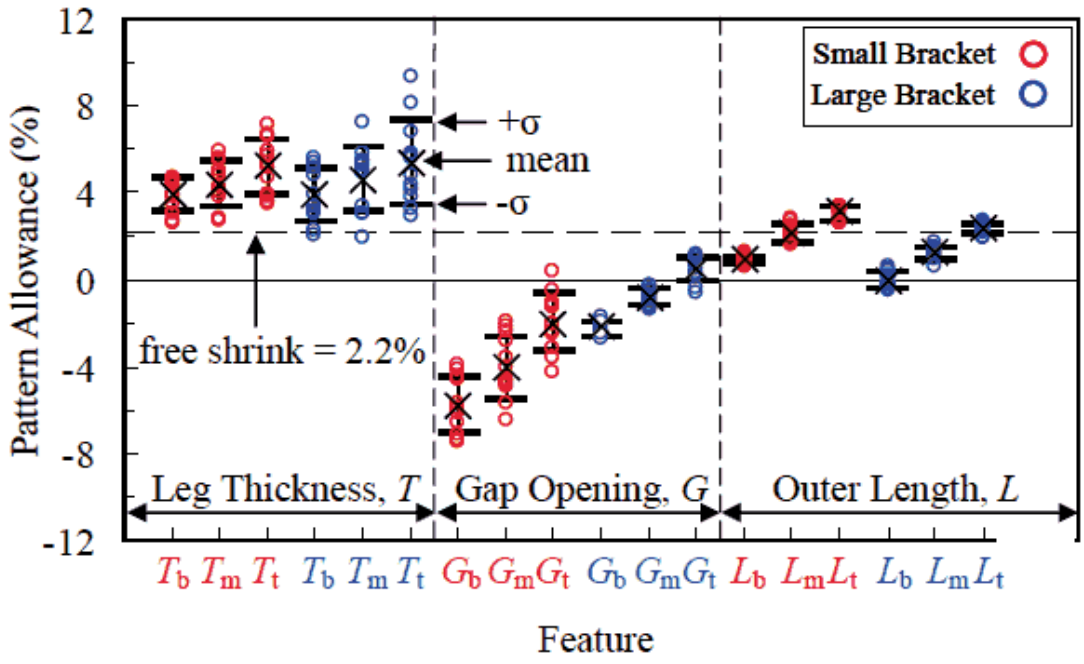

Figure 21. Pattern allowances of the bracket features. The pattern allowances of *T, G,* and *L* (dimensions shown in Figure 4) at the bottom (b), middle (m), and top (t) of the bracket legs characterize the distortions throughout the bracket. Positive pattern allowance represent contraction.

3. Thermophysical Properties and Thermal Simulations

3.1 Thermophysical properties and simulation parameters

A base set of properties and parameters were used to run initial thermal simulations in MAGMAsoft. However, to obtain agreement between measured and simulated temperatures, several adjustments were needed to these base values. The base and final values are shown now and will be discussed in detail in the following section.

Using the average casting chemistry of the four experimental sets, temperature-dependent thermophysical properties of the steel were calculated using IDS[6] software. IDS and adjusted thermophysical properties are shown in Figure 22. Additionally, the volume fraction of solid during solidification as a function of temperature and the latent heat of solidification were calculated in IDS. The IDS and adjusted solid fraction are shown in Figure 23.

Another important parameter of the thermal simulations is the interfacial heat transfer coefficient (IHTC), which characterizes the heat transfer at the mold-metal interface. As the casting cools, thermal contraction of the steel creates a gap at the interface, reducing the rate of heat transfer from the casting to the mold, which results in a decrease of IHTC. For the initial thermal simulation, the "Steel-Sand" dataset from the MAGMAsoft database was used and is shown with the adjusted IHTC in Figure 24.

Finally, the adjusted thermophysical properties of the mold were based off of the "Furan" dataset from the MAGMAsoft database. Both thermophysical property sets are shown in Figure 25.

3.2 Thermal simulations

In order to match the simulated and measured temperatures, virtual thermocouples were created in the MAGMAsoft model at all (steel and mold) experimental thermocouple locations. In addition to the properties and parameters presented in the previous section, the IDS latent heat of solidification of 250 kJ/kg and a pouring temperature of 1600°C were specified to perform initial thermal simulations in MAGMAsoft. Final comparisons between simulated and measured temperatures in the steel and mold for the large bracket are shown in Figures 26 and 27, respectively. Similar comparisons in the steel and mold are shown for the small bracket in Figures 28 and 29, respectively.

Matching simulated and measured temperatures is a multi-step iterative process, which is briefly discussed now. For an in-depth discussion of the process, the interested reader is referred to Carlson and Beckermann[7]. In the first step, a reference time is set, in which the simulated and experimental times are set to zero when the molten steel first contacts the thermocouple. At this time, the simulated thermocouple immediately reads the temperature of the liquid steel. The experimental thermocouple, however, experiences a lag for high temperature gradients and requires several seconds to read the actual temperature, at which time the liquid melt has already cooled by several degrees. For this reason, the simulated steel thermocouple reads a slightly higher temperature than its experimental counterpart.

Next, the temperature curves must agree in the time interval from the maximum temperature until the onset of solidification at the liquidus temperature, T_{liq}. The slopes of the curves in this region are matched first by enhancing the steel thermal conductivity

by a factor of 2.5 above T_{liq}, shown in Figure 22(a). This enhancement accounts for convective heat transfer in the liquid melt and results in a higher cooling rate. The times to T_{liq} are then matched by adjusting the simulated pouring temperature. A higher pouring temperature adds heat to the molten steel and increases the time to the liquidus temperature. The simulated pouring temperature was adjusted from 1600°C to 1610°C for the large and small brackets.

Once the times to T_{liq} have been matched, the temperature curves are matched throughout the solidification range, which is bounded by T_{liq} and the solidus temperature, T_{sol}. The curves within this range are matched by adjustment of the solid fraction curve, shown in Figure 23. Subsequently, the times to T_{sol} are matched by an adjustment to either 1) the latent heat of solidification of the steel or 2) the mold thermal conductivity. Because an adjustment to the mold thermal conductivity significantly affects the temperatures in both the steel and mold, it is important to compare all (steel and mold) temperatures from this time forward. The best agreement in the initial mold temperatures and times to T_{sol} was achieved through adjustments to both the latent heat and thermal conductivity of the mold. The latent heat was reduced from an initial IDS value of 250 kJ/kg to 200 kJ/kg, while the adjustment to the mold thermal conductivity is shown in Figure 25(a). Recall that binder gases are created in the mold as the binder burns away. For this reason, the heat transfer increases due to advection as the binder gases escape out of the porous mold. After the gases have escaped, the heat transfer, which is now due to only conduction, decreases. The effect of the binder gases can be seen in Figure 25(a) as an enhancement of the thermal conductivity at temperatures below 500°C.

At the end of solidification, temperatures are subsequently matched to the beginning the solid state transformation. For small temperature differences, or if the simulation cools too quickly, the IHTC may be altered to achieve agreement. However, for large discrepancies in which the simulated bracket cools too slowly, the thermal conductivity of the mold must be adjusted. This was the case, as adjusted mold thermal conductivity was significantly altered from the original Furan thermal conductivity, shown in Figure 25(a).

As previously explained, the experimental solid state transformations occur at different temperatures ranging from a few degrees to greater than 100°C. For simplicity, the simulated solid state transformations were assumed to occur at the same temperature. In order to simulate this transformation, a spike is required in the specific heat curve at the transformation temperature, which can be seen in Figure 22(c). By changing the magnitude of the spike, the duration of the solid state transformation can be increased or decreased. Agreement was achieved by decreasing the spike by approximately 1000 J/kg-K from the original IDS value.

Finally, the simulated and measured temperatures are matched from the solid state transformation down to room temperature. Adjustments made to the thermal conductivity will alter the simulation at higher temperatures and should be avoided. Therefore, agreement is achieved solely through adjustment of the IHTC. Recall that the mold thermal conductivity was enhanced at low temperatures to account for advection through the mold due to binder gases. This enhancement results in hysteresis of the sand. Clearly, during cooling binder gases are not present and therefore, the thermal conductivity should not be enhanced. As a result, the sand cools too quickly during cooling, which can be seen in Figures 27 and 29. To achieve agreement during cooling,

the mold thermal conductivity must be lowered at temperatures below 500°C. By doing this, however, the agreement in the sand during heating would be sacrificed. This is a limitation of the simulation software. Therefore, it must be decided for which regime (heating or cooling) agreement is most critical. For the present study, the predicted bracket distortions are a strong function of the mold thermal expansion. Therefore, because the temperatures during heating of the mold govern the mold expansion, it is crucial to match the simulated and thermal temperatures during heating. Also, recall that the steel significantly increases in strength during the solid state transformation. As a result, the sand core no longer constrains the steel, resulting in free contraction of the bracket. For this reason, the sand temperatures after the solid state transformation have a negligible effect on bracket distortion. The enhanced mold thermal conductivity at low temperatures also causes the casting to cool too quickly at temperatures below the solid state transformation. However, this can be remedied by artificially decreasing the IHTC at low temperatures, shown in Figure 24.

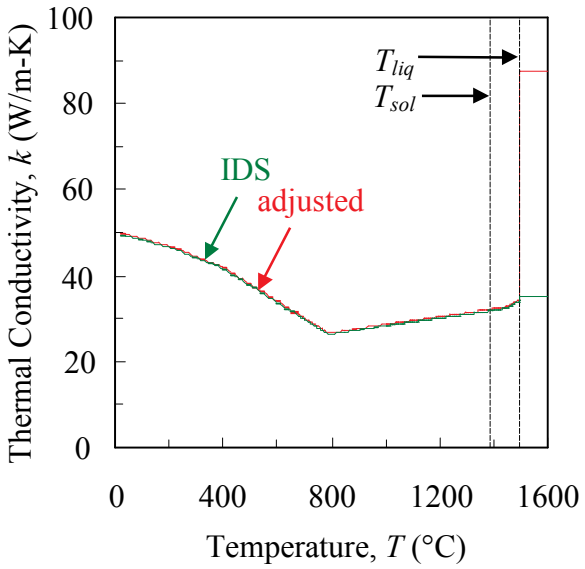

(a) Thermal conductivity

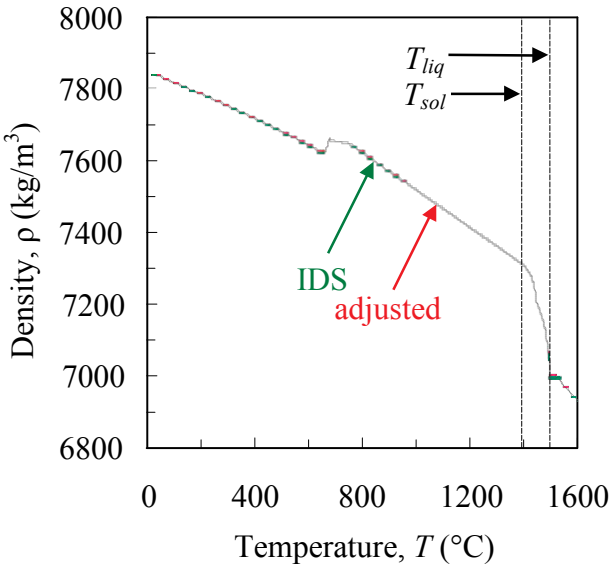

(b) Density

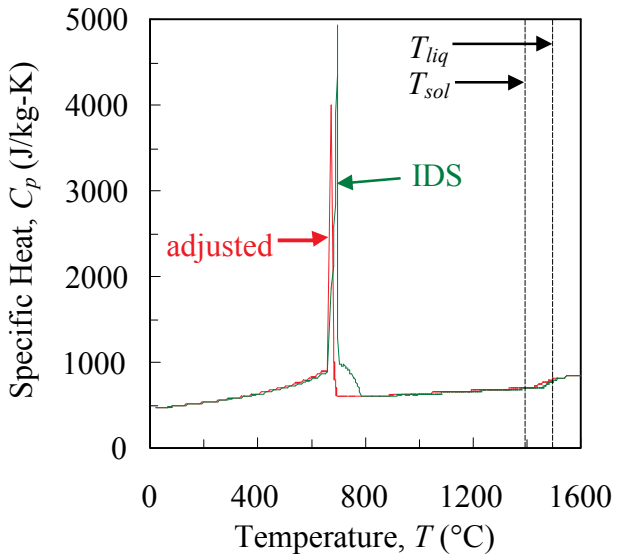

(c) Specific Heat

Figure 22. Steel thermophysical properties. The initial IDS properties, which were calculated using the casting chemistry were used for the initial thermal simulations. The adjusted properties were used in the thermal simulations that gave the best agreement between measured and simulated temperatures.

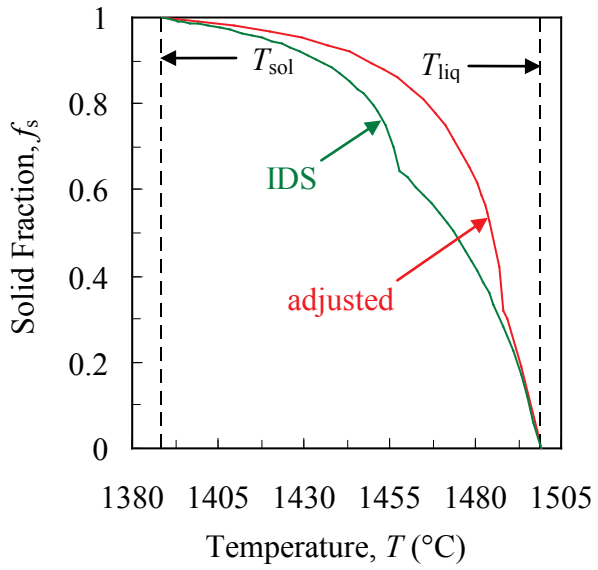

Figure 23. Solid fraction. The IDS solid fraction was calculated using the casting chemistry and used for the initial thermal simulations. The adjusted solid fraction was used in the thermal simulations that gave the best agreement between measured and simulated temperatures.

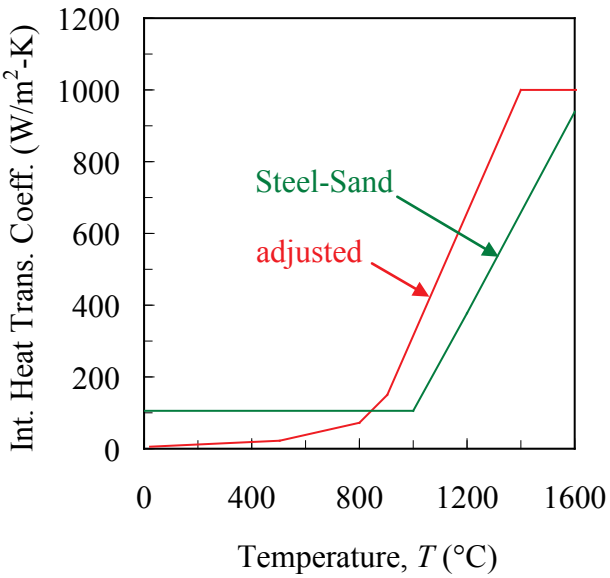

Figure 24. Interfacial heat transfer coefficient. The Steel-Sand IHTC, found in the MAGMAsoft database, was used in the initial thermal simulation. The adjusted IHTC was used in the thermal simulations that gave the best agreement between measured and simulated temperatures.

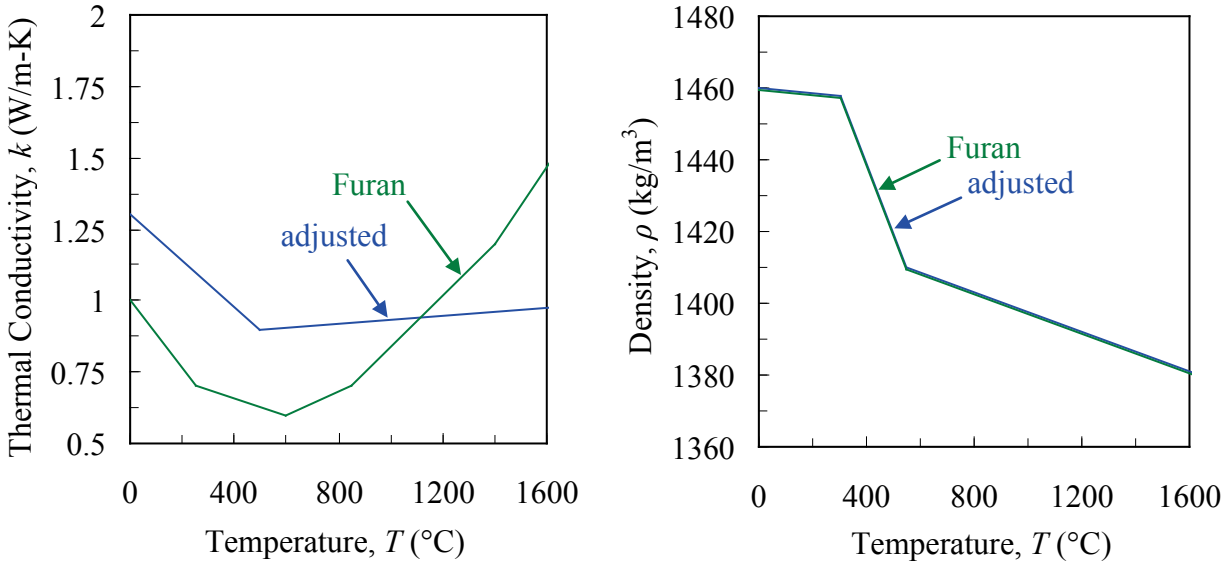

(a) Thermal conductivity

(b) Density

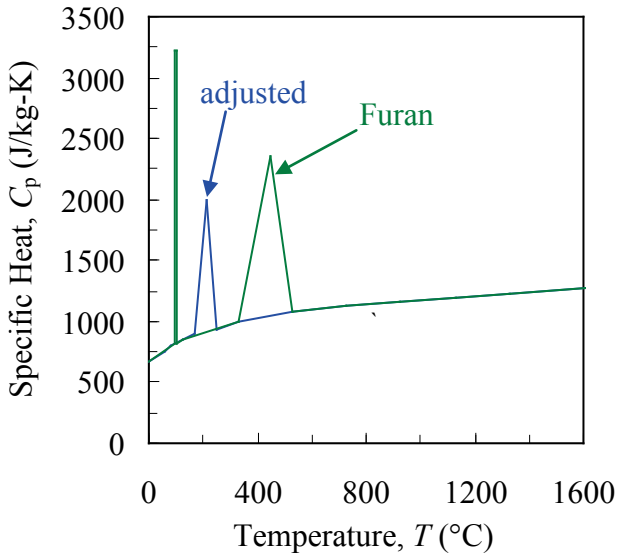

(c) Specific Heat

Figure 25. Mold thermophysical properties. The initial thermal simulations used the mold properties from the Furan dataset, located in the MAGMAsoft database. The adjusted properties were used in the thermal simulations that gave the best agreement between measured and simulated temperatures.

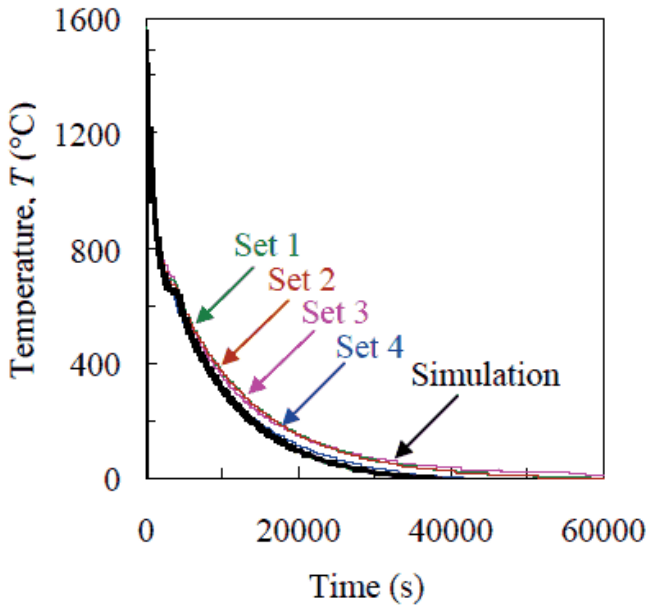

(a) Large time scale.

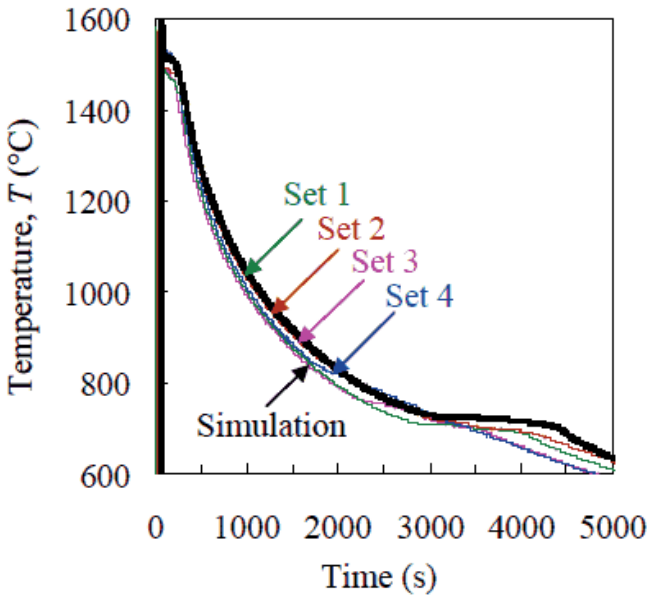

(b) Medium time scale.

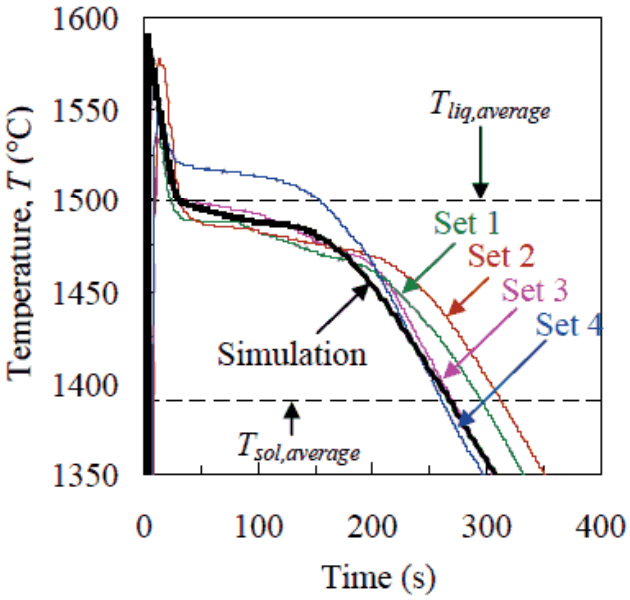

(c) Small time scale.

Figure 26. Comparison of large bracket measured and simulated steel temperatures. Good overall agreement is achieved during solidification and cooling.

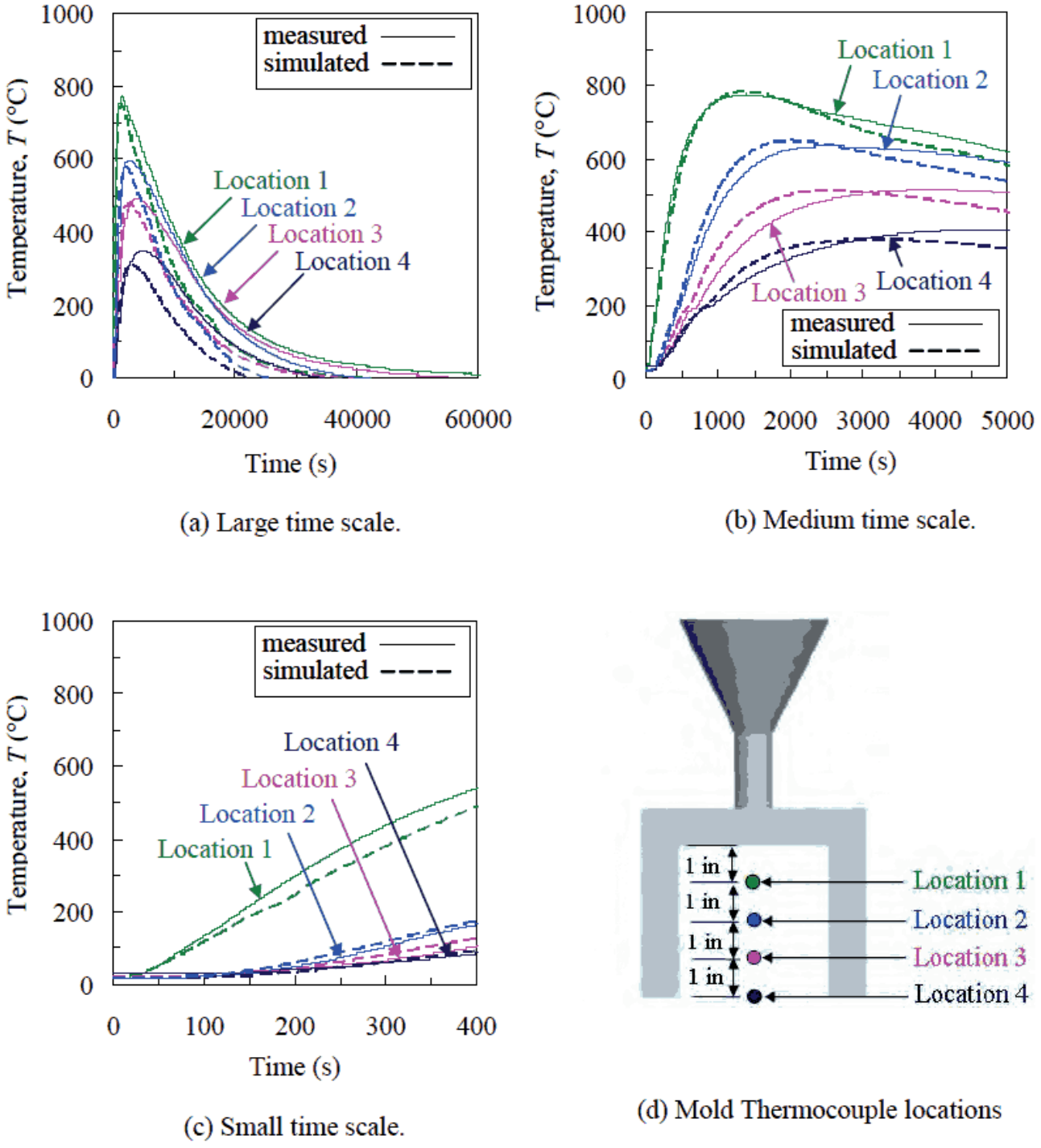

(a) Large time scale.

(b) Medium time scale.

(c) Small time scale.

(d) Mold Thermocouple locations

Figure 27. Comparison of large bracket measured and simulated mold temperatures. Good agreement is achieved during heating, but due to sand hysteresis, the simulated temperatures cool too quickly during cooling.

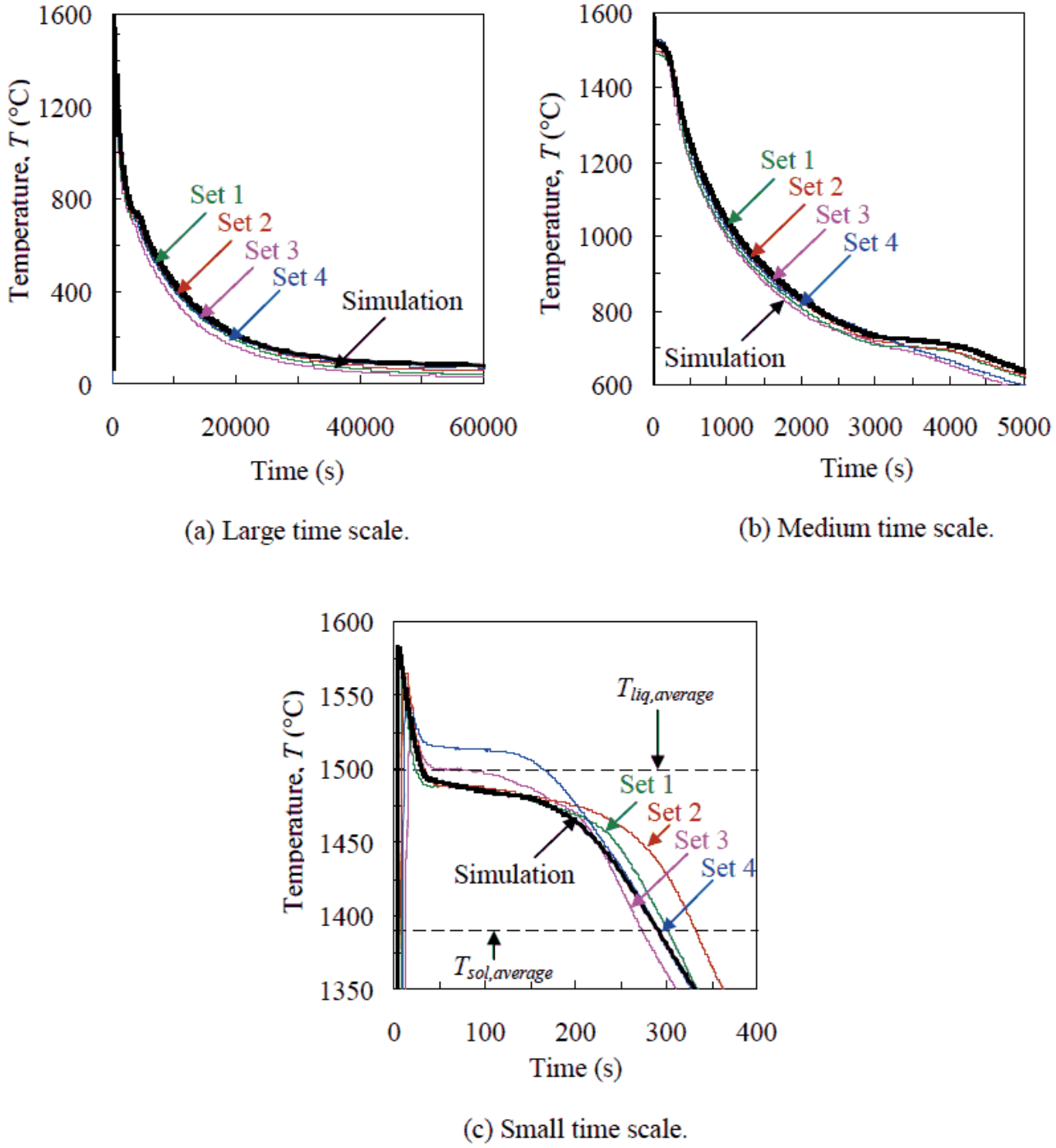

Figure 28. Comparison of small bracket measured and simulated steel temperatures. Good overall agreement is achieved during solidification and cooling.

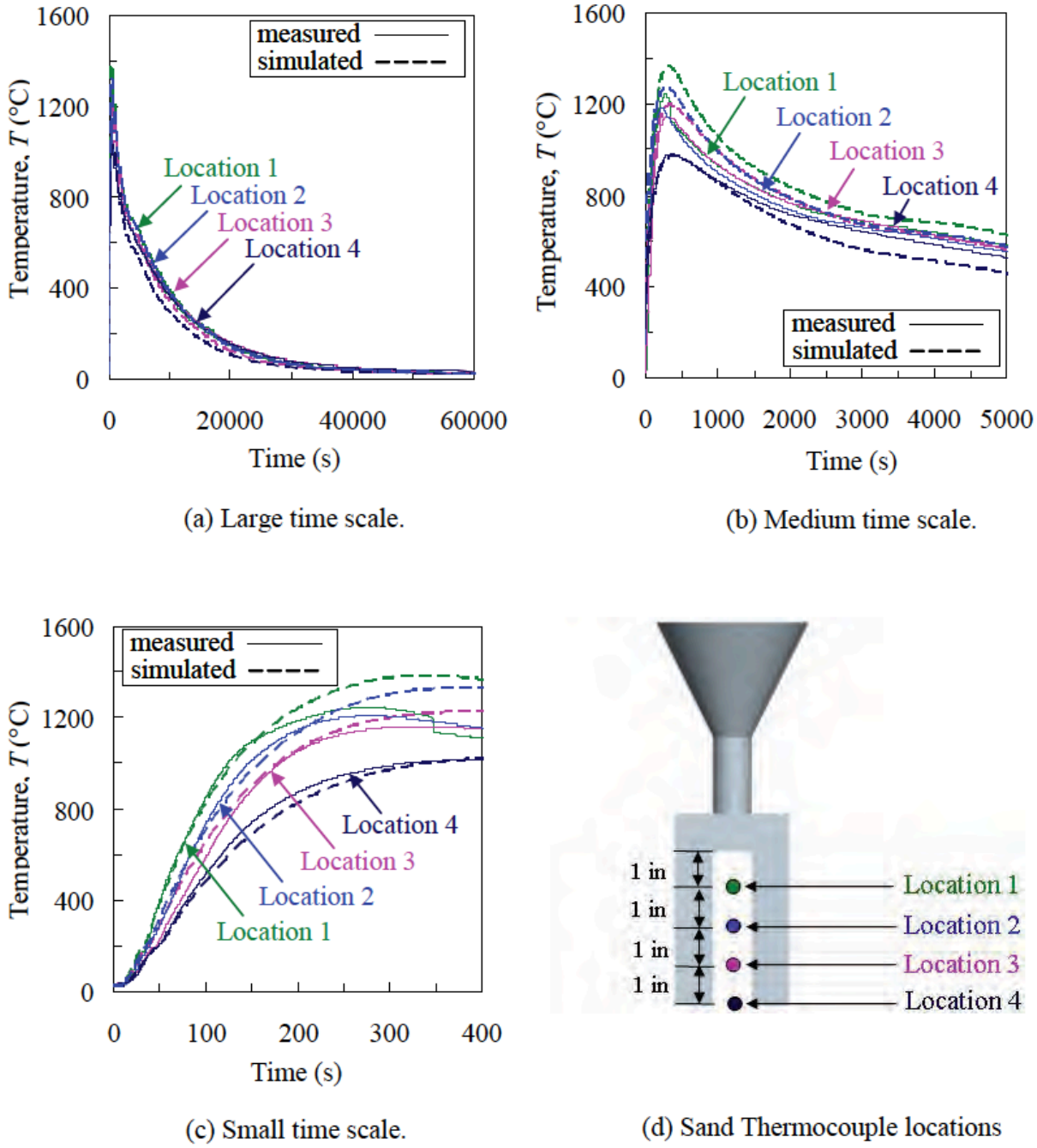

Figure 29. Comparison of small bracket measured and simulated mold temperatures. Good agreement is achieved during heating. The simulated temperatures at locations 1, 2, and 3 reach higher maximum temperatures than in the experiments. Also, due to sand hysteresis, the simulated temperatures cool too quickly during cooling.

4. Stress Model

4.1 Steel

To include the effects of solid deformation, the solid momentum equation must be solved for and is given by

$$\nabla \cdot \boldsymbol{\sigma} = 0 \tag{1}$$

where $\boldsymbol{\sigma}$ is the stress tensor.

Assuming small strain theory, the total strain, $\boldsymbol{\varepsilon}$, can be decomposed into the elastic (e), thermal (th), and viscoplastic (vp) components as

$$\boldsymbol{\varepsilon} = \boldsymbol{\varepsilon}_e + \boldsymbol{\varepsilon}_{th} + \boldsymbol{\varepsilon}_{vp} \tag{2}$$

Using Hooke's law, the elastic strain is determined by

$$\boldsymbol{\sigma} = \boldsymbol{C}_e : \boldsymbol{\varepsilon}_e \tag{3}$$

where $\boldsymbol{C}_e$ is the elastic stiffness tensor. Assuming a homogeneous and isotropic material, $\mathbf{C}_e$ is defined as

$$\boldsymbol{C}_e = \frac{E}{3(1-2\nu)} \boldsymbol{I} \otimes \boldsymbol{I} + \frac{E}{(1+\nu)} \boldsymbol{I}_{dev} \tag{4}$$

where E is Young's modulus, ν is Poisson's ratio, $\boldsymbol{I}$ is the fourth-order identity tensor, and $\boldsymbol{I}_{dev}$ is the fourth-order deviatoric identity tensor.

The thermal strain is given by

$$\boldsymbol{\varepsilon}_{th} = \alpha_{tot}(T - T_{coh})\boldsymbol{1} \tag{5}$$

where T_{coh} is the temperature at which the material reaches coherency and begins to thermally contract, which is generally taken as the solidus temerature. Additionally, $\boldsymbol{1}$ is the second-order identity tensor, and α_{tot} is the total thermal expansion coefficient and defined as

$$\alpha_{tot} = \frac{1}{(T - T_{coh})} \int_{T_{coh}}^{T} -\frac{1}{3\rho_s} \frac{d\rho_s}{dT} dT \tag{6}$$

where ρ_s is the solid density. Equation (6) is the form of the coefficient of thermal expansion required by ABAQUS.

The viscoplastic strain is determined from the flow condition, which limits the maximum stress the material can hold by keeping the equivalent stress less than or equal to the yield stress. When the equivalent stress exceeds the dynamic yield stress, the plastic strain is increased to satisfy $\sigma_{eq} \le \sigma_{dy}$. The equivalent stress is given by

$$\sigma_{eq}^2 = A_1(g_s)q^2 + A_2(g_s)p^2 \tag{7}$$

where q is the von Mises stress and p is the pressure. The functions A_1 and A_2 are from the Cocks model and depend on the solid fraction[8]. In the limit where the solid fraction is unity, equation (7) reduces to the von Mises solution, where A_1 is equal to unity and A_2 is equal to zero.

The dynamic yield stress for the solid material is given by

$$\sigma_{dy} = \sigma_0\left(1+\frac{\varepsilon_{eq}}{\varepsilon_0}\right)^n\left(1+\frac{\dot{\varepsilon}_{eq}}{\dot{\varepsilon}_0}\right)^m \tag{8}$$

where σ_0 is the initial yield stress, ε_{eq} is the equivalent plastic strain, ε_0 is the reference shear strain and given by $\varepsilon_0 = \sigma_0 n/E$, $\dot{\varepsilon}_{eq}$ is the equivalent plastic strain rate, $\dot{\varepsilon}_0$ is the reference strain rate, n is the strain hardening exponent, m is the strain rate sensitivity exponent, and E is Young's modulus.

4.2 Mold

The mold is modeled as an elastic material, and the elastic strain is calculated using equation (3). An additional critical temperature for this model is the degradation temperature, above which the mold loses its strength, and its elastic modulus is reduced to a small value.

The thermal expansion of the mold material is governed by equation (6).

5. Mechanical Properties

Elastic mechanical properties were taken directly from the literature. The temperature-dependent Young's modulus of the steel, taken from Li and Thomas[9], is shown in Fig. 30. For initial stress simulations, a constant elastic modulus of the mold was assumed and taken as the room temperature value of 3754 MPa, as measured by Thole and Beckermann[10]. Also, because experimental observations of increased Poisson's ratio with temperature may be due to increasing amounts of creep during the test[11], a constant value of 0.3 was used for Poisson's ratio for both the steel and mold.

Galles *et al.*[4] estimated the viscoplastic parameters of equation (8) using high-temperature stress-strain data found in the literature. The strain rate sensitivity exponent,

m, and the strain hardening exponent, n, are shown in Figure 31. Below the solid state transformation temperature, T_{sst}, the strain rate sensitivity exponent decreases sharply to zero and results in a rate-independent material. The hardening parameter increases with decreasing temperature from 1600°C until T_{sst}, at which it remains a constant down to room temperature. The initial yield stress (σ_0), shown in Figure 32, characterizes the strength of the material. At temperatures above T_{sst}, the steel is very weak, which is reflected by a low σ_0. However, as the temperature cools to T_{sst}, σ_0 increases sharply, resulting in a dramatic increase in the strength of the steel. The reference strain and strain rates are shown in Figures 31 and 32, respectively. The reference strain can be viewed as a lower limit. Strains that occur below this value are too small to have an effect on hardening of the material. Similarly, strain rates that are lower than the reference strain rate are sufficiently small so that the material does not exhibit rate-dependent behavior.

In addition to the elastic mechanical properties and visco-plastic parameters, thermal expansion coefficients in both the steel and mold are required to calculate thermal strains during the stress simulations. In particular, ABAQUS uses the total thermal expansion coefficient, α_{tot}, which is defined in equation (6) as a function of the density, current temperature, and a reference temperature. The linear thermal expansion and total thermal expansion coefficient for the mold and steel are shown in Figure 33. The linear thermal expansion of the mold is taken from Thiel and Monroe[12], from which the total thermal expansion coefficient was subsequently calculated. Conversely, the total thermal expansion coefficient was calculated from the IDS density using equation (6), from which the linear thermal expansion was calculated. The free shrink line at 0.022 (2.2%) in Figure 33(a) corresponds with the average solidus temperature of all sets.

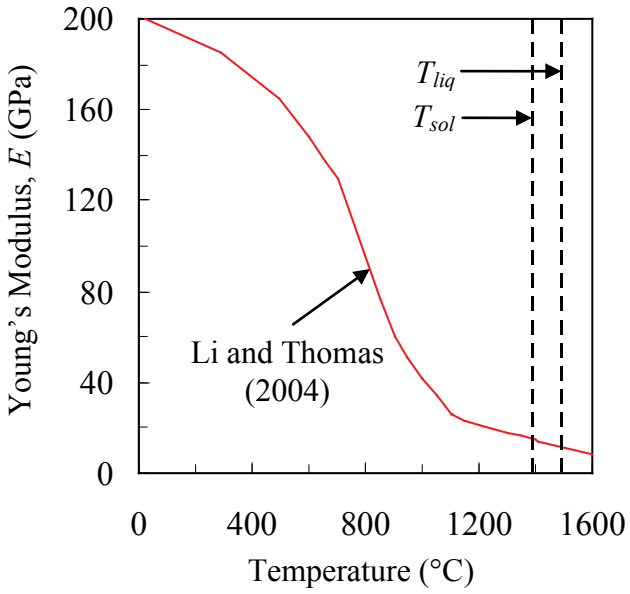

Figure 30. Young's Modulus

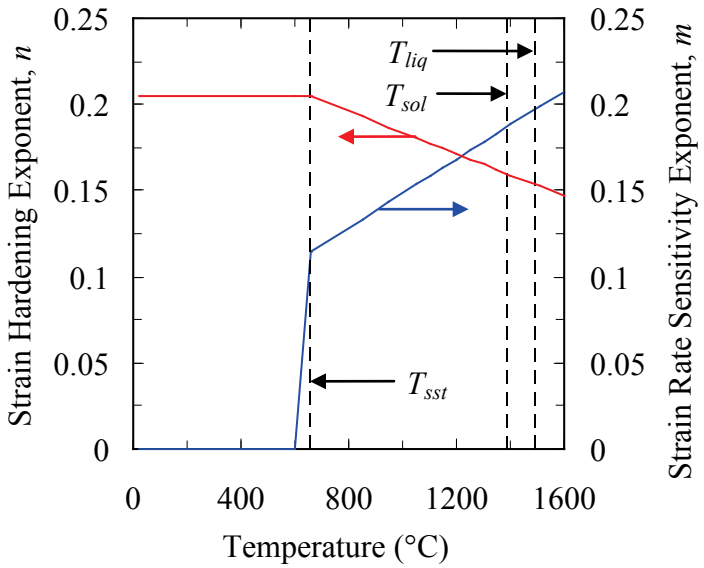

Figure 31. Strain hardening and strain rate sensitivity exponents. Below the solid state transformation temperature, T_{sst}, the strain rate sensitivity exponent decreases sharply to zero, resulting in a rate-independent material.

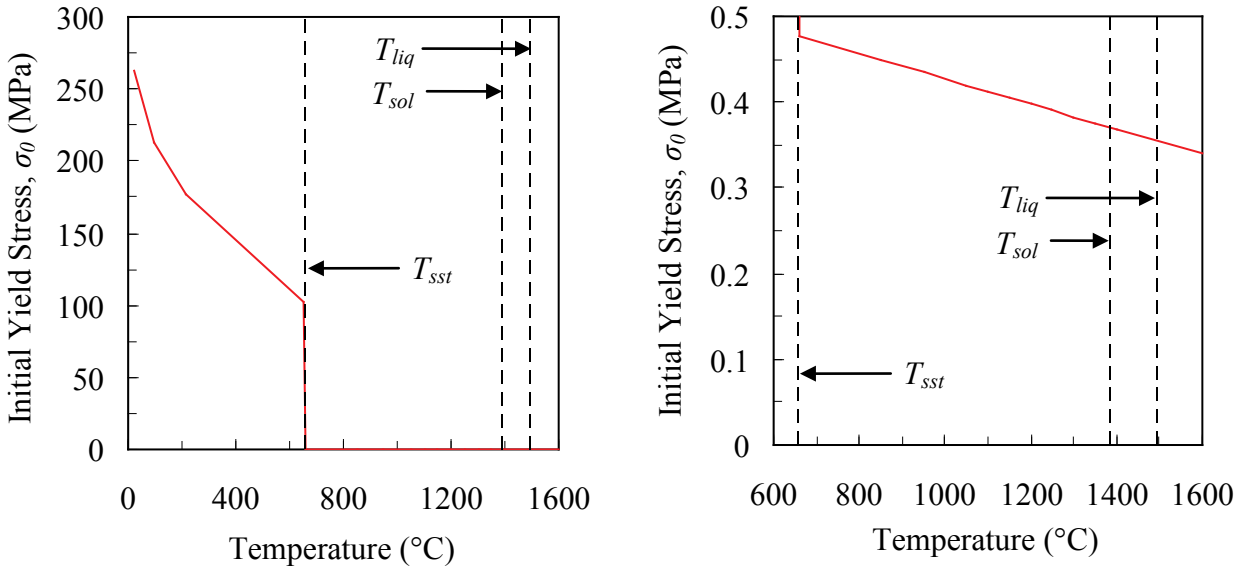

Figure 31. Initial yield stress shown on different stress scales. The sharp increase in the initial yield stress below the solid state transformation temperature, T_{sst}, results in a strength increase of 2-3 orders of magnitude.

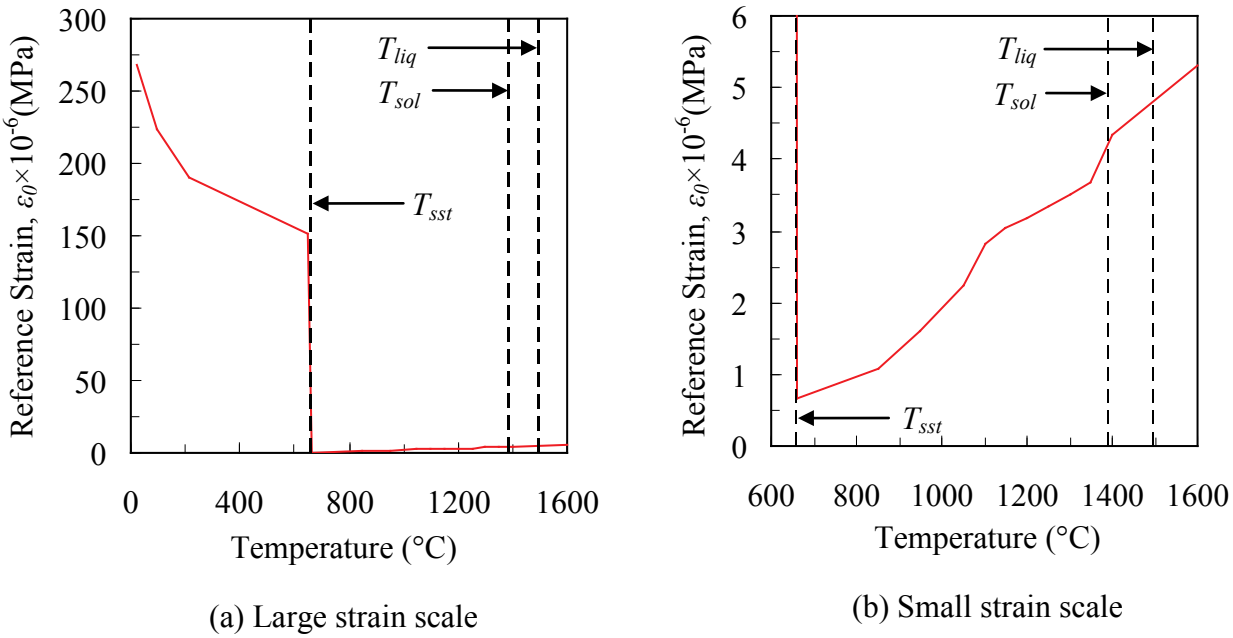

Figure 31. Reference strain shown on different strain scales. As the strain falls below the reference strain, the steel experiences negligible hardening.

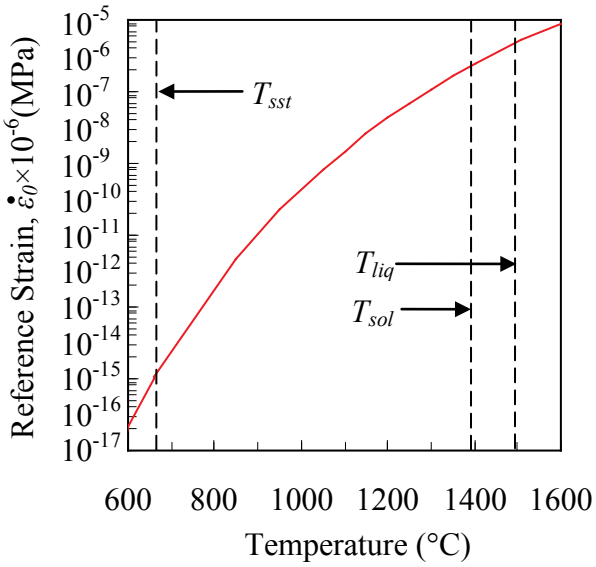

Figure 32. Reference strain rate. As the strain rate is decreased below the reference strain rate, the steel no longer behaves as a rate-dependent material.

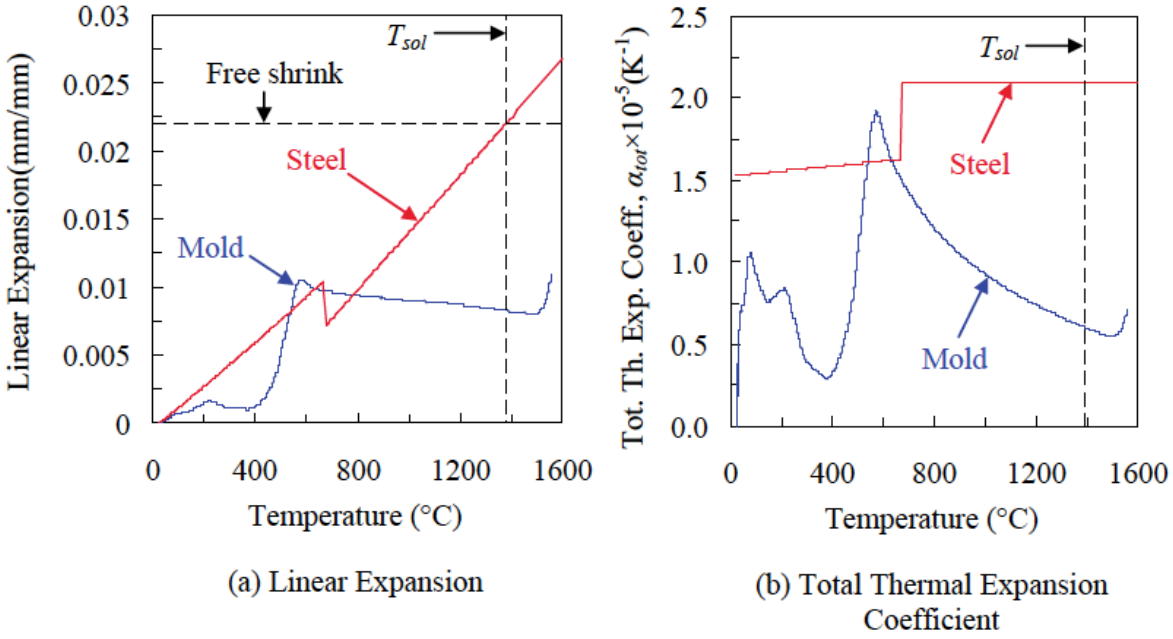

Figure 33. Linear expansion and total thermal expansion coefficient of the mold and steel.

6. Stress Simulations

To perform stress simulations, all properties, parameters, and thermal expansion coefficients explained in the previous section were used as inputs. Additionally, the solid fraction as a function of temperature was required to solve for functions A_1 and A_2 in equation (7). Also, because most properties and parameters are temperature-dependent, temperatures are required at all times and locations in the casting and mold. To obtain these temperatures, thermal fields were calculated in MAGMAsoft at several time steps. Fine time steps were used at high temperatures where the casting cooled quickly, while coarse time steps were used at lower temperatures. In total, thermal fields were calculated at approximately100 time steps. Using MAGMAlink, the thermal fields were then copied from the MAGMAsoft mesh onto the ABAQUS mesh.

From Figure 1, it can be seen that the brackets are symmetric about the two vertical planes. Therefore, to save computational costs, only one-quarter of the bracket was modeled. Additionally, because the steel in the pouring cup does not contribute to stresses and distortions in the bracket, it was also not included in the stress simulations. Because of the difficulty encountered in assigning realistic boundary conditions, a thin outer mold was used for the simulations. By including this outer mold, only stress-free (symmetry) boundary conditions existed on the casting, thus avoiding unrealistic stresses and distortions that may arise from constraining the casting. The downfall of including the outer mold is an increase in computational time. Recall (from the results section) that the outer mold fractured shortly after pouring as the core expanded. Once this fracture occurred, the outer mold lost all strength and no longer contributed to distortions in the bracket. For this reason, the outer mold in ABAQUS was modeled as an elastic material with a very low modulus (10 MPa). Therefore, simulated the outer mold will only act to

keep the bracket in place and not cause distortions. However, the outer mold was still assigned the total thermal expansion coefficient shown in Figure 33(b).

Simulations were performed for both large and small brackets. Additional simulations were performed, in which the cores and outer molds were not included. The results of these simulations will 1) validate the coefficient of thermal expansion in the steel, and 2) be compared to the simulations with cores to reveal the magnitudes of core expansion, and thus, distortions in the casting. Results of the simulations with and without cores for the large bracket are shown in Figure 34. Figure 34(c) shows excellent agreement between the simulation with a core and experimental measurements for the first 400 seconds. The initial decrease in the simulated outer length is due to the initial compression of the outer mold. Even though it has a low modulus, the outer mold is still strong enough to compress the casting while the steel is liquid. The outer length reaches a minimum after approximately 20 seconds and then begins to increase. As it increases, the slopes of the measured and simulated outer lengths are nearly identical. However, after 1000 s, the measured outer length begins to decrease while the simulation continues to increase until approximately 3000 s. At this time, the simulated distortion has more than doubled the measured distortions. After decreasing in outer length for the next 1000 s, the simulation reaches the solid state transformation and increases in outer length for approximately 500 s until decreasing down to room temperature. A comparison between the large bracket simulations with and without cores shows that the core creates a large amount of distortion in the bracket. At 3500 s, the simulated curves reach a maximum distance of nearly 6 mm. Once the steel reaches the solid state transformation and strengthens, however, the core no longer distorts the steel, and as a result, the simulated curves are parallel after the solid state transformation, shown in Figure 34(a). Because of this, the displacement in the bracket after the solid state transformation is only the result of thermal strains in the steel. Figure 34(a) also shows the outer length contraction in the simulation without a core is very close to the free shrink at room temperature, thus validating the accuracy of the thermal expansion coefficient of the steel. The reason for bracket outer length not reaching the free shrink line can be explained by the following. Uneven cooling likely occurs at the tops of the bracket legs to cause distortion, which may “kick” the bracket legs outward. As a result, a larger outer length is measured.

Stress simulations with and without a core for the small bracket are shown in Figure 35. A comparison between the two simulations shows the core has little effect on the small bracket. Initially, the small bracket decreases in outer length for the first 20 seconds. Once again, this is due to the outer mold expansion before the steel solidifies. After that however, the core expansion only slightly pushes the legs outward at 100 s. Because both simulation curves are parallel for the next few hundred seconds. Because of this, it can be concluded that the core creates negligible distortion. The core appears to have an impact on the casting after 1000 s as the simulated curves begin to diverge. However, this effect is small, and the final difference between the simulations with and without a core is less than 0.5 mm. As was the case in the large bracket simulation without a core, the small bracket (without core) simulation predicts a final displacement that is nearly equal to the free shrink.

Von Mises residual stresses and equivalent plastic strains at room temperature are shown for the large and small brackets in Figures 36 and 37, respectively. Because the

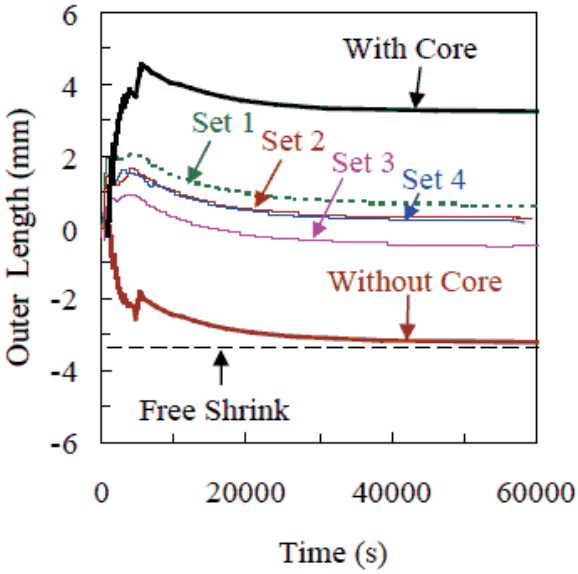

(a) Large time scale.

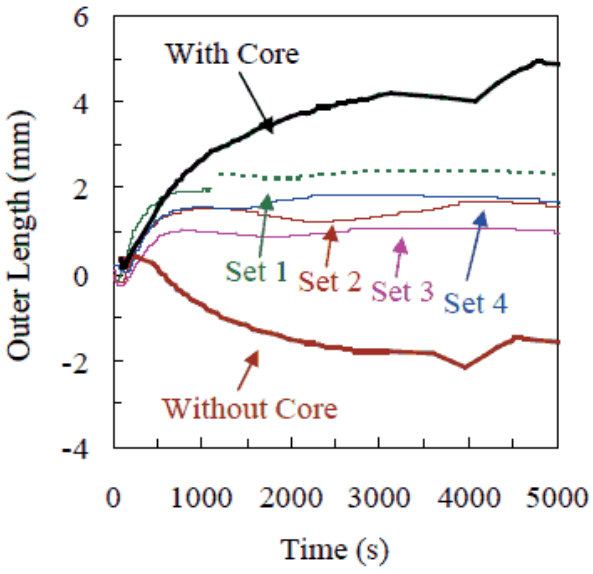

(b) Medium time scale.

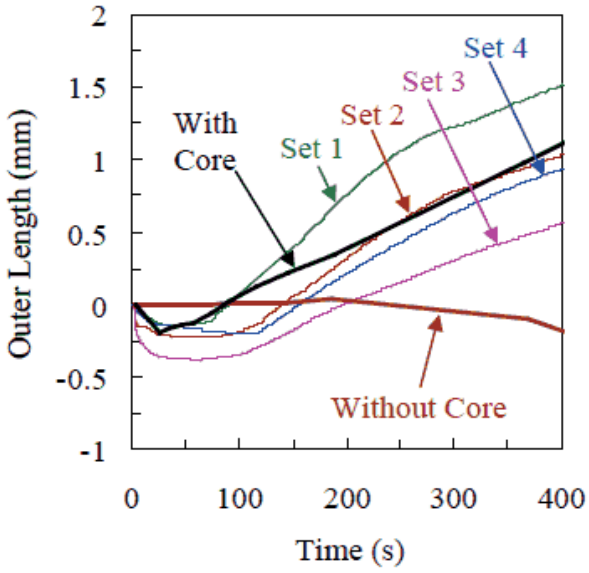

(c) Small time scale.

Figure 34. Comparison of large bracket simulated and measured outer length.

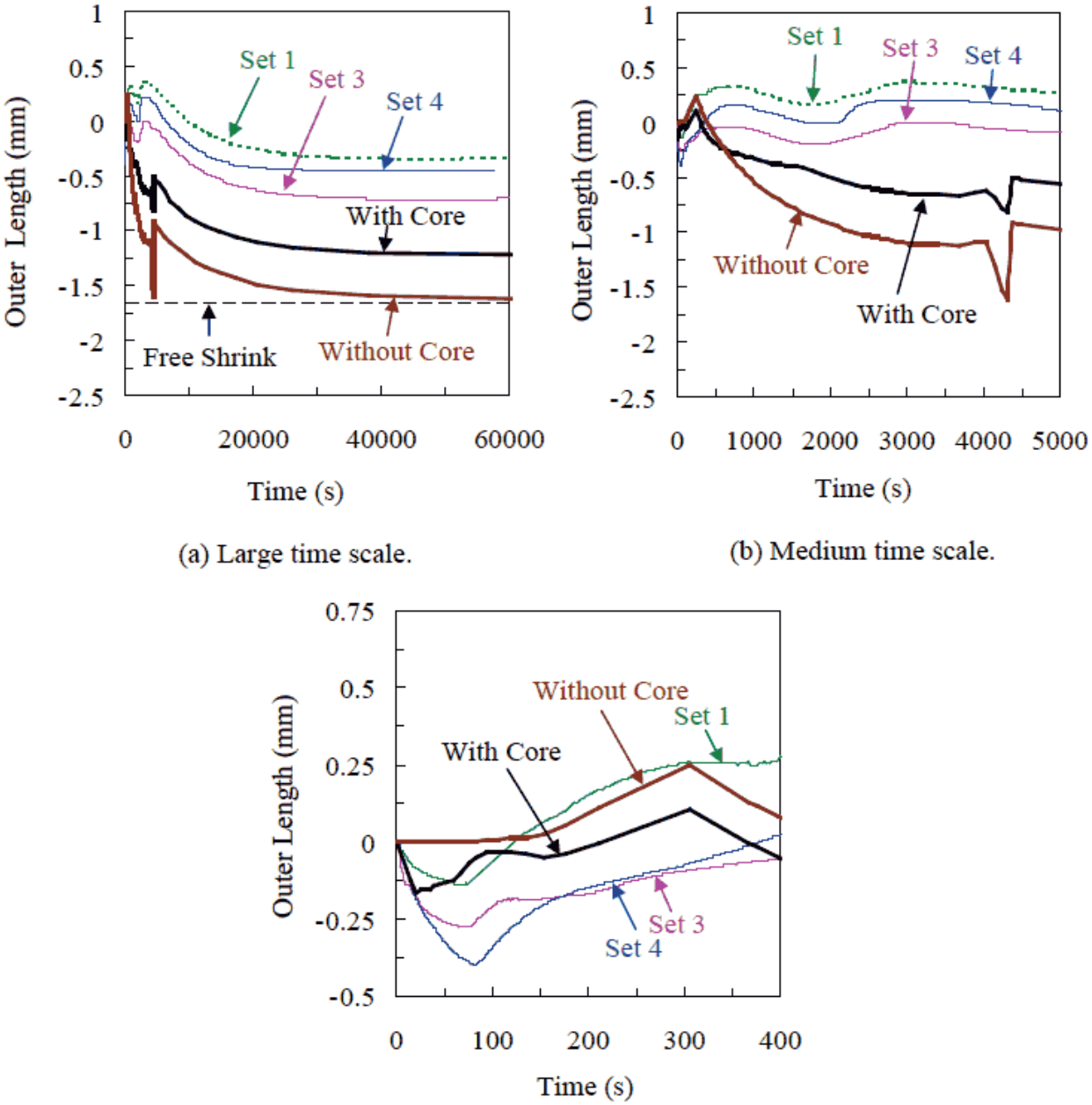

(a) Large time scale.

(b) Medium time scale.

(c) Small time scale.

Figure 35. Comparison of small bracket simulated and measured outer length.

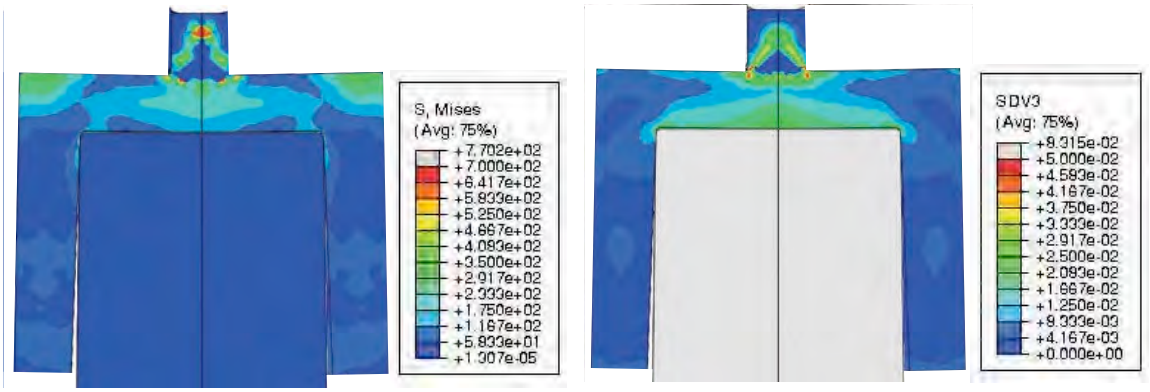

(a) Von Mises Stresses (b) Equivalent Plastic Strain

Figure 36. Von Mises stresses and equivalent plastic strains in the large bracket at room temperature

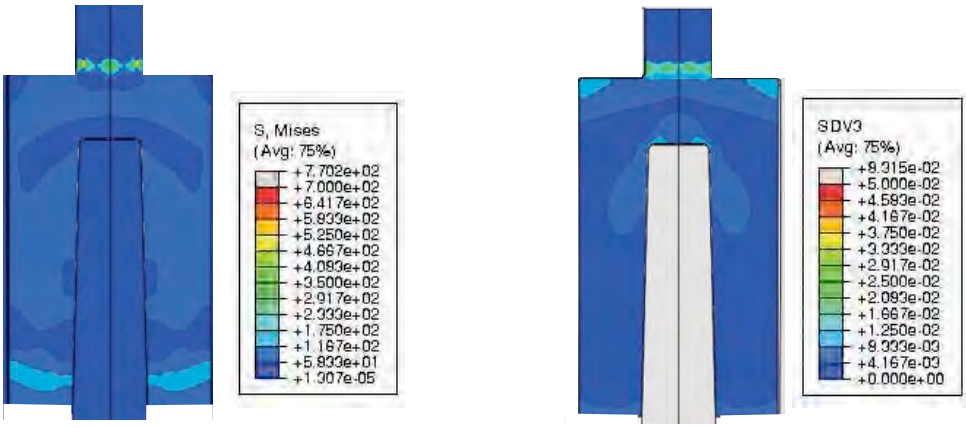

(a) Von Mises Stresses (b) Equivalent Plastic Strain

Figure 37. Von Mises stresses and equivalent plastic strains in the small bracket at room temperature

large bracket simulation predicted much larger distortions than the small bracket simulation, the resulting stresses and plastic strains are also larger in the large bracket, as expected. The majority of the distortion occurs at the top of the large bracket, as shown by the large amounts of plastic strain in Figure 36(b). Also, very few stresses and distortions occur in the large bracket legs. However, (somewhat) higher stresses are seen at the bottom of the legs of the small bracket. Because the small bracket simulations measured negligible distortion, though, the corresponding stresses are most likely inaccurate. For this reason, no conclusions should be made from the stresses (and distortions) in the small bracket.

7. Conclusions and Future Work

In this study, casting distortions were measured during *in situ* experiments for steel brackets with different core sizes. Distortion at the bottom of the bracket legs was measured as a function of time during solidification and cooling. Mold measurements and final casting measurements after shakeout were taken of several casting features to determine pattern allowances. Thermal fields of the bracket during cooling were calculated and the results were transferred to an FEM mesh. Using the material properties acquired through a search of the literature, stress simulations were performed to predict distortions in the brackets. Preliminary results show excellent initial agreement between measured and predicted distortions of the large bracket. At later times, however, the simulation predicts higher distortions than what were measured in the experiments. The small bracket simulation, conversely, predicts very little distortion when compared to the experiments. Because the distortion is a strong function of core expansion, the mold properties must be studied in further detail. In particular, the thermal expansion of the mold requires scrutiny.

Acknowledgements

Special thanks to Jerry Thiel and the students from the Metal Casting Center at the University of Northern Iowa for their assistance with the casting experiments.

References

1. *MAGMAsoft*, MAGMA GmbH, Kackerstrasse 11, 52072 Aachen, Germany.

2. *Abaqus/Standard*, Abaqus, Inc., Providence, RI, 2006.

3. Bichler, L., Elsayed, A., Lee, K., and Ravindran, C., "Influence of Mold and Pouring Temeratures on Hot Tearing Susceptibility of AZ91D Magnesium Alloy", *International Journal of Metalcasting*, vol. 2, no. 1, pp 45-56, 2008.

4. Galles, D., Monroe, C., and Beckermann, C., "Measurement and Prediction of Stresses during Casting of a Steel Bar", *Proceedings of the 65th Technical and Operating Conference*, paper no. 5.5, Steel Founders Society of America, Chicago, IL, 2011.

5. Monroe, C., and Beckermann, C., "Development of a Hot Tear Indicator for Steel Castings", *Materials Science and Engineering A*, vol. 413-414, pp 30-36, 2005.

6. J. Miettinen, "Calculation of Solidification-related Thermophysical Properties for Steels", *Metallurgical and Materials Transactions B*, vol. 28, no. 2, pp 281-297, April 1997.

7. Carlson, K.D., Beckermann, C., ”Development of Thermophysical Property Datasets, Benchmark Niyama Results, and a Simulation Qualification Procedure”, *Proceedings of the 64th Technical and Operating Conference*, paper no. 5.5, Steel Founders Society of America, Chicago, IL, 2010.

8. Marin, E.B., and McDowell, D.L., “A Semi-implicit Integration Scheme for Rate-dependent and Rate-independent Plasticity”, *Computers and Structures*, vol. 63, no.3, pp 30-36, 2005.

9. Chunsheng Li and Brian G. Thomas, “Thermomechanical Finite-element Model of Shell Behavior in Continuous Casting of Steel”, *Metallurgical and Materials Transactions B*, vol. 35B, pp 1151-1172, December 2004.

10. Thole, J., and Beckermann, C., “Measurement of Elastic Modulus of PUNB Bonded Sand as a Function of Temperature”, *Int. J. Metalcasting*, vol. 4, no. 4, pp 7 – 18, 2010.

11. Brian G. Thomas, “Issues in Thermal-mechanical Modeling of Casting Processes”, *ISIJ International*, vol. 35, no. 6, pp 737-743, 1995.

12. Thiel, J., Monroe, C.A., “High Temperature Physical Properties of Chemically Bonded Sands with Applications using Simulation”, *Proceedings of the 64th Technical and Operating Conference*, Steel Founders Society of America, Chicago, IL, 2010.